SIAM J. SCI. COMPUT.
Vol. 43, No. 2, pp. A1027–A1061

A TRULY EXACT PERFECT ABSORBING LAYER FOR TIME-HARMONIC ACOUSTIC WAVE SCATTERING PROBLEMS*

ZHIGUO YANG†, LI-LIAN WANG‡, AND YANG GAO§

Abstract. In this paper, we design a truly exact perfect absorbing layer (PAL) for domain truncation of the two-dimensional Helmholtz equation in an unbounded domain with bounded scatterers. This technique is based on a complex compression coordinate transformation in polar coordinates and a judicious substitution of the unknown field in the artificial layer. Compared with the widely used perfectly matched layer (PML) methods, the distinctive features of PAL lie in that (i) it is truly exact in the sense that the PAL-solution is identical to the original solution in the bounded domain reduced by the truncation layer; (ii) with the substitution, the PAL-equation is free of singular coefficients and the substituted unknown field is essentially nonoscillatory in the layer; and (iii) the construction is valid for general star-shaped domain truncation. By formulating the variational formulation in Cartesian coordinates, the implementation of this technique using standard spectral-element or finite-element methods can be made easy as a usual coding practice. We provide ample numerical examples to demonstrate that this method is highly accurate and robust for very high wavenumbers and thin layers. It outperforms the classical PML and the recently advocated PML using unbounded absorbing functions. Moreover, it can fix some flaws of the PML approach.

Key words. perfect absorbing layer, perfectly matched layer, compression coordinate transformation, substitution, high-order methods

AMS subject classifications. 65N35, 65N22, 65F05, 35J05

DOI. 10.1137/19M1294071

1. Introduction.

Many physical and engineering problems involving wave propagations are naturally set in unbounded domains. Accurate simulation of such problems becomes exceedingly important in a variety of applications. Typically, the first step is to reduce the unbounded domain to a bounded domain so that most of the finite-domain solvers can be applied. The reduced problem should be well-posed, and the underlying solution must be as close as possible to the original solution in the truncated domain. As such, the development of efficient and robust domain truncation techniques has become a research topic of longstanding interest. Several notable techniques have been intensively studied in the literature, which particularly include the artificial boundary conditions (ABCs) (see, e.g., [3, 21, 22, 25, 30, 43, 32]) and artificial absorbing (or sponge) layers (see, e.g., [4, 14, 5, 6, 16, 51]).

In regards to the former approach, the local ABCs are easy to implement, but they can only provide low-order accuracy with undesirable reflections at times. Alternatively, domain truncation based on the Dirichlet-to-Neumann (DtN) map, gives

*Submitted to the journal's Methods and Algorithms for Scientific Computing section October 18, 2019; accepted for publication (in revised form) December 28, 2020; published electronically March 16, 2021.

https://doi.org/10.1137/19M1294071

Funding: The work of the first author was partially supported by the Strategic Priority Research Program of Chinese Academy of Sciences grant XDA25010402. The work of the second author was partially supported by Singapore MOE AcRF Tier 2 Grants MOE2018-T2-1-059 and MOE2017-T2-2-144.

†School of Mathematical Sciences, Shanghai Jiao Tong University, Shanghai, 200240, China (yangzhiguo@sjtu.edu.cn).

‡Corresponding author. Division of Mathematical Sciences, School of Physical and Mathematical Sciences, Nanyang Technological University, 637371, Singapore (lilian@ntu.edu.sg).

§Division of Mathematical Sciences, School of Physical and Mathematical Sciences, Nanyang Technological University, 637371, Singapore (GAOY0032@e.ntu.edu.sg).

rise to an equivalent boundary-value problem, so it is transparent (or equivalently nonreflecting). However, such an ABC is nonlocal in both space and time, which brings about substantial complexity in implementation. Moreover, its analytic series representation (in space) is available only for the artificial boundary/surface being of a simple geometry (circle or ellipse in two dimensions, and sphere or ellipsoid in three dimensions). As such, much effort is needed to seamlessly integrate DtN ABC with curvilinear spectral elements in two dimensions (cf. [24, 55, 56]), but the extension to three dimensions is highly nontrivial (cf. [52]). The coupling of the DtN ABC with the boundary perturbation/field expansion techniques has proven to be successful for solving scattering problems with relatively general bounded scatterers and artificial surfaces (cf. [38, 39, 40]). It is also noteworthy that with a good trade-off between accuracy and efficiency, the high-order ABCs without high-order derivatives become appealing [26], and the double absorbing boundary method appears to be a very intriguing notion [31, 45].

Pertinent to the latter approach, the perfectly matched layer (PML) first proposed by Bérenger [4, 5, 6] essentially builds upon surrounding bounded scatterers by an artificial layer of finite width. The artificial layer is filled with fictitious absorbing media that can attenuate the outgoing waves inside. Since these pioneering works of Bérenger, the PML technique has become a widespread tool for various wave simulations, undergone in-depth analysis of its mathematical ground (see, e.g., [35, 10, 11, 12] and the references cited therein), and been populated into major software such as COMSOL Multiphysics. In the past decade, this subject area has continued to inspire new developments—just to name a few: [7, 8, 23, 19, 50, 18]. Remarkably, the essential idea of constructing PML [4] can be interpreted as a complex coordinate stretching (or transformation) [14, 16]. Consider, for example, the circular PML in polar coordinates for the two-dimensional Helmholtz problem [16, 10], where the domain of interest is truncated and surrounded by an artificial annulus of width d, with the assumption that the inhomogeneity of the media and scatterers are enclosed by a circle C_R of radius R. The corresponding (radial) complex coordinate transformation that generates the anisotropic media inside the annular layer is of the form

$$\tilde{r} = r + \mathrm{i}\int_R^r \sigma(s)\,\mathrm{d}s, \quad R < r < R + d, \tag{1.1}$$

where $\sigma(s) > 0$ is called the *absorbing function* (ABF). Note that the Helmholtz problem inside C_R remains unchanged, i.e., $\tilde{r} = r$. One typical choice of the ABF is

$$\sigma(s) = \sigma_0 (s - R)^n / d^n, \quad n = 0, 1, \ldots, \tag{1.2}$$

where $\sigma_0 > 0$ is a tuning parameter. The PML truncates the domain at a finite distance and attenuates the wave (i.e., the original solution) in the annular layer by enforcing the homogeneous Dirichlet boundary condition at the outer boundary $r = R + d$, where some artificial reflections are usually induced. In theory, the reflection can be a less important issue based on the fundamental analysis (see, e.g., [35, 16, 10]). Lassas and Somersalo [35] showed that the PML-solution converges to the exact solution exponentially when the thickness of the layer tends to infinity. As pointed out by Collino and Monk [16], it is important to optimally choose the parameters to reduce the potentially increasing error in the discretization. The use of adaptive techniques can significantly enhance the performance of PML as advocated by Chen and Liu [10]. It is noteworthy that the complex coordinate transformation (1.1)–(1.2) is also used in developing the uniaxial PML in Cartesian coordinates along

each coordinate direction [49, 12, 13]. However, Singer and Turkel [49] demonstrated that such a transformation is less effective for the evanescent waves in the waveguide setting. Recently, Zhou and Wu [58] proposed to combine the PML with few-mode DtN truncation to deal with the evanescent wave components. It is noteworthy that according to [33, 37, 23], the PML has flaws and failures at times.

An intriguing advancement is the "exact" and "optimal" PML using *unbounded* ABFs $\sigma(\cdot)$ (see (2.15) and (3.23) below), developed by Bermúdez et al. [7, 8] for the time-harmonic acoustic wave scattering problems. Indeed, it was shown in [44, 46] through sophisticated comparison with the classical PML that it can be "parameter-free" and has some other advantages. However, according to the error analysis in [49] (also see Theorem 2.1), this technique fails to be exact for the waveguide problem but can improve the accuracy of the classical PML. On the other hand, the unbounded ABFs lead to PML-equations with singular coefficients so much care is needed to deal with the singularities, in particular, for high wavenumbers and thin layers.

In this paper, we propose a truly exact perfect absorbing layer with general star-shaped domain truncation of the exterior Helmholtz equation in an unbounded domain. In the spirit of our conference paper [53], its construction consists of two indispensable building blocks:

(i) Different from (1.1), we use a complex compression coordinate transformation of the form $\tilde{r} = \rho(r) + \mathrm{i}(\rho(r) - R)$. Here $\rho(r)$ is a real mapping that compresses $\rho \in (R, \infty)$ into $r \in (R, R + d)$ along the radial direction.

(ii) We introduce a suitable substitution of the field in the artificial layer, $U = wV$, where w extracts the essential oscillation of U, and also includes a singular factor to deal with the singular coefficients (induced by the coordinate transformation) of the resulting PAL-equation. The field V to be approximated is well-behaved in the layer. We formulate the variational form of the PAL-equation (designed in polar coordinates) in Cartesian coordinates, so it is friendly for the implementation with the finite-element or spectral-element solvers.

We remark that the use of compression coordinate transformation is inspired by the notion of an "inside-out" invisibility cloak [57] where a real rational mapping was used to compress an open space into a finite cloaking layer. However, this cloaking device is far from perfect (cf. [53]). To generate a perfect cloaking layer, we employ the complex compression mapping like the complex coordinator stretching in PML, in order to attenuate the compressed outgoing waves. Notably, we can show the truncation by the PAL is truly exact in the sense that the PAL-solution is identical to the original solution in the inner domain (exterior to the scatterer but inside the inner boundary of the artificial layer). The substitution in (ii) turns out to be critical for the success of the PAL technique for the reasons that this can overcome the numerical difficulties of dealing with singular coefficients of the PAL-equation and remove the oscillations near the inner boundary of the layer. Indeed, both the analysis and ample numerical evidence show that the new PAL method is highly accurate even for high wavenumber and thin layers.

The rest of the paper is organized as follows. In section 2, we present the essential idea of PAL using a waveguide problem in a semi-infinite domain. A delicate error estimate has been derived for the PML and PAL methods, and a comparison study has been conducted of PAL and PML with regular and unbounded ABFs. In section 3, we start with a general set-up for the star-shaped truncated domain for exterior wave scattering problems and provide new perspectives of the circular PAL reported in [53]. In section 4, we provide in detail the construction of the PAL-equation based

on the complex compression coordinate transformation and the variable substitution technique used to eliminate the oscillation and singularity. In section 5, ample numerical experiments are provided to demonstrate the performance of the PAL method and show its advantages over the PML methods.

2. Waveguide problem in a semi-infinite channel. In this section, we elaborate on the essential idea of the new PAL and compare it with the classical PML (cf. [4, 14, 16, 49]) and the "exact" and "optimal" PML techniques using unbounded (singular) ABFs (cf. Bermúdez et al. [7, 8]) in the waveguide setting. Indeed, such a relatively simpler context enables us to conduct a precise error analysis and better understand the significant differences between two approaches.

To this end, we consider the semi-infinite x-aligned waveguide from $x = 0$ to $x = \infty$ (see Figure 1 (left)), governed by the Helmholtz equation (cf. [49, 44]):

$$\mathscr{L}[U] := \Delta U + k^2 U = 0 \quad \text{in} \quad \Omega_\infty := \big\{0 < x < \infty,\ 0 < y < \pi\big\}; \tag{2.1a}$$

$$U(x,0) = U(x,\pi) = 0, \quad x \in [0,\infty); \quad U(0,y) = g(y), \quad y \in [0,\pi], \tag{2.1b}$$

where the wavenumber $k > 0$, the field U is outgoing, and $g \in L^2(0,\pi)$. We refer to Goldstein [27, (2.2)] for the outgoing radiation condition:

$$U(x,y) = \sum_{l=1}^{\infty} \hat{c}_l\, e^{\mathrm{i}\hat{k}_l x} \sin(ly) \quad \text{and} \quad \frac{\partial U}{\partial x} = \sum_{l=1}^{\infty} \mathrm{i}\hat{k}_l\, \hat{c}_l\, e^{\mathrm{i}\hat{k}_l x} \sin(ly) \tag{2.2}$$

for each $x \geq x_1 > 0$ and $y \in (0,\pi)$, where $\hat{k}_l := \sqrt{k^2 - l^2}$ and $\{\hat{c}_l\}$ can be determined by given Dirichlet data at any given $x_1 > 0$. Note that (2.2) implies the DtN boundary condition

$$\frac{\partial U}{\partial x} = \mathcal{T}[U] := \sum_{l=1}^{\infty} \mathrm{i}\hat{k}_l\, \widehat{U}_l\, e^{\mathrm{i}\hat{k}_l x} \sin(ly) \quad \text{at} \quad x = x_1,$$

where $\{\widehat{U}_l\}$ are the Fourier sine coefficients of U at $x = x_1$. Using the Fourier sine expansion in the y-direction, we find readily that the problem (2.1)–(2.2) admits the series solution:

$$U(x,y) = \sum_{l=1}^{\infty} \hat{g}_l\, e^{\mathrm{i}\hat{k}_l x} \sin(ly) \quad \text{with} \quad \hat{g}_l = \frac{2}{\pi} \int_0^{\pi} g(y) \sin(ly)\, \mathrm{d}y. \tag{2.3}$$

2.1. The PML technique and its error analysis. To solve (2.1) numerically, one commonly used approach is the PML technique which reduces the semi-infinite

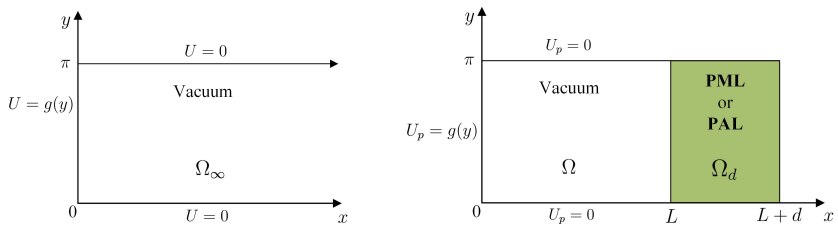

FIG. 1. *Left: schematic diagram of x-aligned semi-infinite waveguide. Right: domain reduction by an artificial layer using the PML or PAL technique.*

strip Ω_∞ in (2.1) to a rectangular domain $\Omega := (0, L) \times (0, \pi)$ by appending an artificial layer $\Omega_d := (L, L+d) \times (0, \pi)$ with a finite thickness d (see Figure 1 (right)). Typically, the artificial layer Ω_d is filled with fictitious absorbing (or lossy) media that can attenuate the waves propagating into the layer. In practice, one would wish the layer could diminish the pollution (due to the reflection) of the original solution in the "physical domain" Ω and its thickness d could be as small as possible to save computational cost.

The critical issue is to construct the governing equation in Ω_d. It is known that the PML-equation can be obtained from the Helmholtz equation $(\Delta + k^2)U = 0$ in $(\tilde{x}, \tilde{y})$-coordinates through complex coordinate stretching (see, e.g., [16, 49]). More precisely, we introduce the complex coordinate transformation of the form

$$\begin{cases} \tilde{x} = S(x), \quad \tilde{y} = y, \quad \forall\, (x, y) \in \Omega \cup \Omega_d \quad \text{such that} \\ S(x) = x \ \ \forall\, x \in (0, L); \ \ \Re\{S'(x)\} > 0, \ \ \Im\{S'(x)\} > 0 \ \forall\, x \in (L, L+d), \end{cases} \tag{2.4}$$

where $S(x)$ is a differentiable complex-valued function. One typically chooses

$$S(x) = x + \frac{\mathrm{i}}{k} \int_0^x \sigma(t)\, \mathrm{d}t \quad \forall\, x \in (0, L+d), \tag{2.5}$$

where $\sigma(\cdot) \geq 0$ is the ABF. Then the substitution

$$\frac{\partial}{\partial x} \to \frac{\partial}{\partial \tilde{x}} = \frac{dx}{d\tilde{x}} \frac{\partial}{\partial x} = \frac{1}{S'(x)} \frac{\partial}{\partial x} \tag{2.6}$$

leads to the PML-equation (cf. [49, (5)])

$$\frac{\partial}{\partial x} \left(\frac{1}{S'(x)} \frac{\partial U_{\mathrm{p}}}{\partial x} \right) + \frac{\partial}{\partial y} \left(S'(x) \frac{\partial U_{\mathrm{p}}}{\partial y} \right) + k^2 S'(x) U_{\mathrm{p}} = 0 \quad \forall\, (x, y) \in \Omega \cup \Omega_d, \tag{2.7}$$

which is supplemented with the transmission conditions at the interface $x = L$,

$$U_{\mathrm{p}}\big|_{\Omega} = U_{\mathrm{p}}\big|_{\Omega_d}, \quad \frac{\partial U_{\mathrm{p}}}{\partial x}\bigg|_{\Omega} = \frac{1}{S'(x)} \frac{\partial U_{\mathrm{p}}}{\partial x}\bigg|_{\Omega_d}, \tag{2.8}$$

together with the boundary conditions,

$$\begin{aligned} &U_{\mathrm{p}}(x, 0) = U_{\mathrm{p}}(x, \pi) = 0, \quad x \in (0, L+d); \\ &U_{\mathrm{p}}(0, y) = g(y), \quad U_{\mathrm{p}}(L+d, y) = 0, \quad y \in (0, \pi). \end{aligned} \tag{2.9}$$

It is noteworthy that with a suitable choice of the ABF $\sigma(t)$, the PML-solution decays sufficiently fast in the artificial layer, so the homogeneous Dirichlet boundary condition is usually imposed at $x = L + d$.

Singer and Turkel [49] conducted error analysis of the PML with the usual bounded ABFs. Here, we provide a much more precise description of the error between the original solution U and the PML-solution U_{p} in the physical domain Ω.

THEOREM 2.1. *Let U be the solution of (2.1) given by (2.3), and let U_{p} be the PML-solution of (2.7)–(2.9). If $k > 0$ is not an integer, then for any $(x, y) \in \Omega$,*

$$U(x, y) = U_{\mathrm{p}}(x, y) + \sum_{l=1}^{\infty} \hat{g}_l\, R_l(x)\, e^{\mathrm{i}\hat{k}_l x} \sin(ly), \quad R_l(x) := \frac{1 - e^{-2\mathrm{i}\hat{k}_l x}}{1 - e^{-2\mathrm{i}\hat{k}_l S_d}}. \tag{2.10}$$

If $k > 0$ is an integer, then $R_l(x)$ for the mode $l = k$ in (2.10) *should be replaced by*

$$R_l(x) = -\frac{S(x)}{S_d} \quad \forall\, x \in (0, L). \tag{2.11}$$

Here, $\hat{k}_l := \sqrt{k^2 - l^2}$, $S_d := S(L + d)$ and $S(x)$ is given in (2.4)–(2.5).

Moreover, we have the bounds (i) *for $0 \le l < k$,*

$$\frac{2|\sin(\hat{k}_l x)|}{e^{2\hat{k}_l \Im\{S_d\}} + 1} \le |R_l(x)| \le \frac{2|\sin(\hat{k}_l x)|}{e^{2\hat{k}_l \Im\{S_d\}} - 1} \quad \forall\, x \in (0, L), \tag{2.12}$$

and (ii) *for $l > k$,*

$$\frac{e^{2|\hat{k}_l| x} - 1}{e^{2|\hat{k}_l| \Re\{S_d\}} + 1} \le |R_l(x)| \le \frac{e^{2|\hat{k}_l| x} - 1}{e^{2|\hat{k}_l| \Re\{S_d\}} - 1} \quad \forall\, x \in (0, L). \tag{2.13}$$

To avoid distraction from the main results, we sketch the proof in Appendix A. We see that for fixed k, l, the decay rate of $R_l(x)$ is completely determined by the values of $\Re\{S_d\}$ and $\Im\{S_d\}$, i.e., the choice of ABF $\sigma(t)$. We now apply Theorem 2.1 to assess the performance of PML with some typical ABFs:

$$\text{PML}_n: \qquad \sigma(x) = \begin{cases} 0 & \text{if } \ x \in (0, L), \\ \sigma_0 \left(\dfrac{x - L}{d}\right)^n & \text{if } \ x \in (L, L + d), \end{cases} \tag{2.14}$$

and

$$\text{PML}_\infty: \qquad \sigma(x) = \begin{cases} 0 & \text{if } \ x \in (0, L), \\ \dfrac{\sigma_0\, d}{L + d - x} & \text{if } \ x \in (L, L + d), \end{cases} \tag{2.15}$$

where $\sigma_0 > 0$ is a tunable constant. We remark that PML_n with integer $n \ge 0$ is commonly used (see, e.g., [16, 49, 10]), while PML_∞ was first introduced by Bermúdez et al. [7, 8] (which was advocated for its being "optimal," "exact," and "parameter-free" in various settings (cf. [7, 8, 44, 42, 15])). It is clear that in Ω_d, we have

$$\text{PML}_n\colon S(x) = x + \frac{\mathrm{i}}{k}\frac{d\,\sigma_0}{n+1}\left(\frac{x - L}{d}\right)^{n+1}, \ \ \Re\{S_d\} = L + d, \ \ \Im\{S_d\} = \frac{\sigma_0\, d}{(n+1)k}, \tag{2.16}$$

and

$$\text{PML}_\infty:\ S(x) = x + \frac{\mathrm{i}\, d\,\sigma_0}{k} \ln\left(\frac{d}{L + d - x}\right), \quad \Re\{S_d\} = L + d, \quad \Im\{S_d\} \to \infty. \tag{2.17}$$

Observe that in both cases, $\Re\{S_d\}$ does not depend on the choice of ABF $\sigma(t)$. Consequently, the main factor in the error $\hat{g}_l R_l(x) e^{\mathrm{i}\hat{k}x}$ of the lth mode, corresponding to the evanescent wave components (i.e., $l > k$), behaves like

$$|R_l(x)| \sim e^{-2\sqrt{l^2 - k^2}(L + d - x)} \quad \forall\, x \in (0, L), \tag{2.18}$$

so the only possibility to reduce the error is to increase the width d.

For the oscillatory wave components (i.e., $l < k$), the PML_∞ can make the factor $R_l(x)$ vanish, but for the PML_n,

$$|R_l(x)| \sim 2\big|\sin\big(\sqrt{k^2-l^2}\,x\big)\big| e^{-2\sqrt{k^2-l^2}\sigma_0\, d/((n+1)k)} \quad \forall\, x \in (0, L), \tag{2.19}$$

so one has to enlarge the thickness d of the layer or choose large σ_0 to reduce the error.

As an illustrative example, we consider the exact solution (2.1) with $\{\hat{g}_l = \mathrm{i}^l J_l(k)\}$ (in order to mimic the plane wave expansion):

$$U(x,y) = \sum_{l=1}^{\infty} \mathrm{i}^l J_l(k) e^{\mathrm{i}\sqrt{k^2-l^2}x} \sin(ly), \tag{2.20}$$

where $J_l(\cdot)$ is the Bessel function. Define the error function:

$$\mathcal{E}_{\mathrm{p}}(x,y) = U(x,y) - U_{\mathrm{p}}(x,y) = \sum_{l=1}^{\infty} \mathrm{i}^l J_l(k)\, R_l(x)\, e^{\mathrm{i}\sqrt{k^2-l^2}x} \sin(ly) \tag{2.21}$$

for all $(x,y) \in \Omega$. Here, we take $k = 9.99, L = 1, d = 0.1$, and truncate the infinite series for $l \le 100$ so that the truncation error is negligible. The error curves $|\mathcal{E}_{\mathrm{p}}(x,y)|$ with fixed $x = L/2, L$ and $y \in (0,\pi)$ in Figure 2 with PML_2 and PML_∞ in (2.14)–(2.15).

Observe from Figure 2 that the errors of the PML_2 become slightly smaller as σ_0 increases, but they are still large. The PML_∞ using unbounded ABFs performs relatively better but does not significantly improve the classical PML.

Remark 2.2. The recent work [58] introduced the few-mode DtN technique to deal with the evanescent wave components, while the other modes were treated with the classical PML_n.

Remark 2.3. As shown in [7], the PML_∞ can completely damp the planar waves of the form $e^{\mathrm{i}k_x x + \mathrm{i}k_y y}$ with $k_x = k\cos\theta_0, k_y = k\sin\theta_0$, where θ_0 is the incident angle at the left boundary $x = 0$ of the half-plane waveguide: $\Delta u + k^2 u = 0,\ x > 0,\ -\infty < y < \infty$. We also refer to [15] for some other successful scenarios. However, it fails to be "exact" and "optimal" in this setting.

Remark 2.4. Note from (2.17) that for the PML_∞, $S'(x) = 1 + \mathrm{i}\,\sigma(x)/k \to \infty$ as $x \to L + d$, so the coefficients in (2.7) are singular at the outer boundary $x = L + d$.

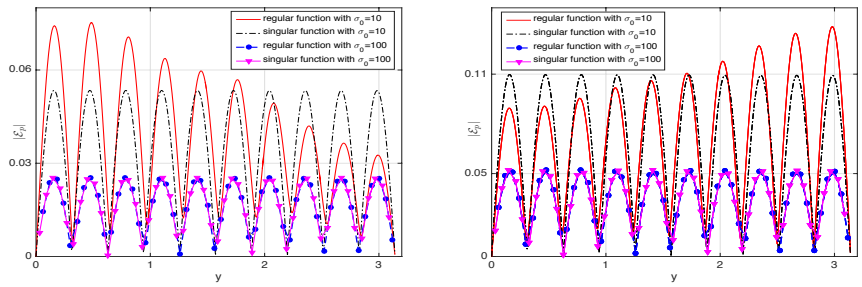

FIG. 2. *Profiles of the error function* $|\mathcal{E}_p(x,y)|$ *of the solution* (2.20) *with* $k = 9.99, L = 1, d = 0.1$, *and* $\sigma_0 = 10, 100$ *using PML*$_2$ *and PML*$_\infty$. *Left: the error curve* $|\mathcal{E}_p(L/2,y)|$ *for* $y \in (0,\pi)$. *Right: the error curve* $|\mathcal{E}_p(L,y)|$ *for* $y \in (0,\pi)$.

In [7, 8], the use of, e.g., Gauss quadrature to avoid sampling the unbounded endpoints was suggested for evaluating the matrices of the linear system in finite-element discretization. However, for large wavenumber k and very thin layer, much care is needed to deal with the singularity to achieve high order. Moreover, in more complex situations, e.g., the circular/spherical PML, $S(x)$ also appears in the PML-equation, so the logarithmic singularity poses even more challenges in numerical discretization.

2.2. New PAL technique and its error analysis. As reported in [53], the new PAL was inspired by the design of the "inside-out" invisibility cloak (cf. [57]) using the notion of transformation optics (cf. [41]). In [57], the real rational transformation was introduced to construct the media and design the clocking layer,

$$\rho = \rho(x) = L + \frac{d(x-L)}{L+d-x}, \quad x \in (L, L+d), \quad \rho \in (L, \infty), \tag{2.22}$$

which compresses the outgoing waves in the infinite strip $\rho > L$ into the finite layer $(L, L+d)$. However, it is known that any attempt of using a real compression coordinate transform fails to work for Helmholtz and Maxwell's equations. Indeed, according to [33], "any real coordinate mapping from an infinite to a finite domain will result in solutions that oscillate infinitely fast as the boundary is approached—such fast oscillations cannot be represented by any finite-resolution grid, and will instead effectively form a reflecting hard wall."

To break the curse of infinite oscillation, we propose the complex compression coordinate transformation ($\mathrm{C^3T}$), that is, $S(x) = x$ for $x \in (0, L)$, and

$$S(x) = S_R(x) + \mathrm{i}\, S_I(x), \quad x \in (L, L+d), \tag{2.23}$$

where the real part $S_R(x) = \sigma_1 \rho(x)$ and the imaginary part $S_I(x) = \sigma_0(\rho(x) - L)/k$. Like (2.15), the imaginary part $S_I(x)$ involves an unbounded ABF:

$$S_I(x) = \frac{1}{k}\int_L^x \sigma(t)\,\mathrm{d}t, \quad \sigma(x) = \sigma_0 \left(\frac{d}{L+d-x}\right)^2, \quad x \in (L, L+d). \tag{2.24}$$

For clarity, we denote the PAL-solution by U_{a}. Thanks to (2.6), we obtain the PAL-equation as the counterpart of (2.7)–(2.9):

$$\begin{aligned} &\frac{\partial}{\partial x}\left(\frac{1}{S'(x)}\frac{\partial U_{\mathrm{a}}}{\partial x}\right) + \frac{\partial}{\partial y}\left(S'(x)\frac{\partial U_{\mathrm{a}}}{\partial y}\right) + k^2 S'(x) U_{\mathrm{a}} = 0, \quad (x,y) \in \Omega \cup \Omega_d, \\ &U_{\mathrm{a}}\big|_{\Omega} = U_{\mathrm{a}}\big|_{\Omega_d}, \quad \frac{\partial U_{\mathrm{a}}}{\partial x}\bigg|_{\Omega} = \frac{1}{S'(x)}\frac{\partial U_{\mathrm{a}}}{\partial x}\bigg|_{\Omega_d} \quad \text{at} \quad x = L, \\ &U_{\mathrm{a}}(x,0) = U_{\mathrm{a}}(x,\pi) = 0; \quad U_{\mathrm{a}}(0,y) = g(y), \;\; U_{\mathrm{a}}(L+d,y) = 0. \end{aligned} \tag{2.25}$$

Importantly, we can show that the new PAL is truly exact and nonreflecting.

THEOREM 2.5. *Let U be the solution of* (2.1) *and U_{a} be the solution of* (2.25). *Then we have*

$$U_{\mathrm{a}}(x,y) \equiv U(x,y) \quad \forall\, (x,y) \in \Omega. \tag{2.26}$$

Proof. Note that the error formula in Theorem 2.1 is valid for general $S(x)$. It is evident that by (2.23), we have $\Re\{S(L+d)\} = \infty$ and $\Im\{S(L+d)\} = \infty$. Thus, it follows immediately from (2.12)–(2.13) that $R_l(x) = 0$ uniformly for all l and $x \in (0, L)$, which implies $U_{\mathrm{a}}(x,y) \equiv U(x,y)$ in Ω. ∎

Different from PML, the truncation by the new PAL is exact at the continuous level, but the compression coordinate transformation induces singular coefficients at $x = L + d$ in the PAL-equation (2.25), which brings about some numerical difficulties in discretization. To overcome this, we introduce the substitution of the unknown:

$$U_{\rm a}(x,y) = w(x)V_{\rm a}(x,y), \quad w(x) = \frac{L+d-x}{d}, \quad x \in (L, L+d), \tag{2.27}$$

with $w(x) = 1$ for $x \in (0, L)$. In fact, the transformed PAL-equation in the new unknown V_a is free of singularity. To show this, it's more convenient to work with the variational form. Denote

$$\mathbb{U} := \big\{u = wv : v \in H^1(\Omega \cup \Omega_d),\ v(x,0) = v(x,\pi) = 0,\ \ x \in (0, L+d)\big\},$$

and introduce the sesquilinear form on $\mathbb{U} \times \mathbb{U}$:

$$\mathcal{B}(U_{\rm a}, \Psi) = (\boldsymbol{C}\,\nabla U_{\rm a}, \nabla\Psi) - k^2(S'\,U_{\rm a}, \Psi), \tag{2.28}$$

where $\boldsymbol{C} = \mathrm{diag}(1/S'(x), S'(x))$, and $(\cdot,\cdot)$ is the inner product of $L^2(\Omega \cup \Omega_d)$.

In view of (2.24), direct calculation leads to $w^2(x)S'(x) = \alpha = \sigma_1 + \mathrm{i}\sigma_0/k$. Then, substituting $U_{\rm a} = wV_{\rm a}$ and $\Psi = w\Phi$ into (2.28), we obtain from direct calculation that

$$\widetilde{\mathcal{B}}_{\Omega_d}(V_{\rm a}, \Phi) = \mathcal{B}_{\Omega_d}(wV_{\rm a}, w\Phi) = (\widetilde{\boldsymbol{C}}\,\widetilde{\nabla}V_{\rm a}, \widetilde{\nabla}\Phi)_{\Omega_d} - \alpha k^2 (V_{\rm a}, \Phi)_{\Omega_d}, \tag{2.29}$$

where $(\cdot,\cdot)_{\Omega_d}$ is the inner product on the artificial layer Ω_d, and

$$\widetilde{\boldsymbol{C}} = \mathrm{diag}\big(w^2(x)/\alpha,\ \alpha\big), \quad \widetilde{\nabla} = \big(w(x)\partial_x - 1/d, w(x)\partial_y\big). \tag{2.30}$$

It is seen from (2.29)–(2.30) that the multiplication of a linear polynomial $w(x)$ in the substitution (2.27) can eliminate the singular factors in the coefficients of (2.28). In principle, one can use a polynomial factor of higher degree. However, it is undesirable to have an additional weight function in the k^2-term of (2.29), and in computation, this may increase the bandwidth of the sparse, banded linear system, e.g., resulting from a spectral approximation. In real implementation, one can easily incorporate the substitution into the basis functions and directly approximate $U_{\rm a}$.

We conclude this section with some numerical results. Consider (2.1) with $k = 29.9$ and the boundary source term is prescribed as $g(y) = \sin(5y) - \sin(30y)$ in (2.1b). The semi-infinite strip Ω_∞ in (2.1) is reduced to a rectangular domain $\Omega := (0,1) \times (0,\pi)$ by appending the PAL layer $\Omega_d := (1, 1+d) \times (0,\pi)$ with a finite thickness d (see Figure 1 (right)).

In the numerical tests, we use a Fourier sine spectral method in y (with a cut-off number M) and a two-domain Legendre spectral method in x (with N_0 and N terms in $(0,1)$ and $(1,1+d)$, respectively), based on the sesquilinear form (2.29)–(2.30). Numerical results obtained by PAL ($\sigma_0 = \sigma_1 = 1$) are also compared with the PML technique with bounded and unbounded ABFs, i.e., PML_n ($n = 1$, $\sigma_0 = 10$) and PML_∞ ($\sigma_0 = 10$) in (3.22)–(3.23), respectively. Here, we take $M = 30$ and $N_0 = 70$ so that the solutions are well-resolved in the interior domain, and the error is largely dominant by the approximation in the artificial layer. In Figure 3, we depict the L^∞-errors for the numerical solution with these three truncation methods. It can be seen that the errors of the PAL method decrease exponentially to 10^{-10} as N increases. However, due to the existence of evanescent modes, the errors saturated at around 10^{-1} and 10^{-2} for PML method with $d = 0.1$ and $d = 0.5$, respectively. As analyzed previously, the saturation level can be improved only by an increased layer thickness d, which is prohibitive due to the increased computational cost.

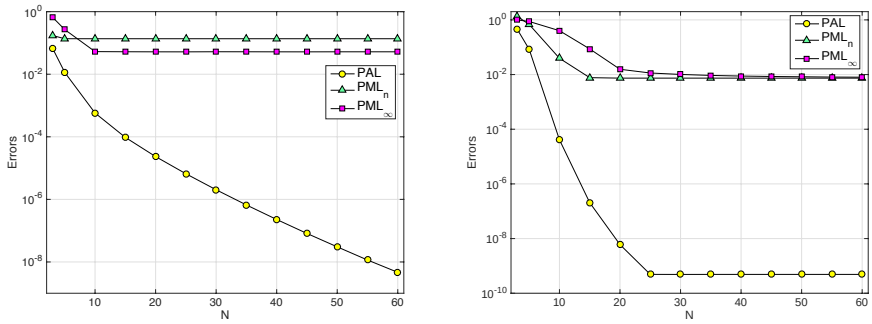

(a) $d = 0.1$ (b) $d = 0.5$

FIG. 3. *A comparasion study for waveguide problem: error for PAL, PML_n, and PML_∞ against N for $k = 29.9$ with different layer thickness* (a) $d = 0.1$ *and* (b) $d = 0.5$.

3. Star-shaped domain truncation and circular PAL. One of the main purposes of this paper is to design the PAL with a general star-shaped domain truncation for solving the two-dimensional time-harmonic acoustic wave scattering problems. More precisely, we consider the exterior domain:

$$\mathscr{L}[U] := \Delta U + k^2 U = f \quad \text{in} \quad \Omega_e := \mathbb{R}^2 \setminus \bar{D}; \tag{3.1a}$$

$$U = g \quad \text{on} \quad \partial D; \qquad \Big|\frac{\partial U}{\partial r} - \mathrm{i}kU\Big| \le \frac{c}{r} \quad \text{for} \quad r =: |\boldsymbol{x}| \gg 1, \tag{3.1b}$$

where $D \subset \mathbb{R}^2$ is a bounded scatterer with Lipschitz boundary $\Gamma_D = \partial D$, and $g \in H^{1/2}(\Gamma_D)$. Here, we assume that the source f is compactly supported in a disk $B(\supset D)$. The far-field condition in (3.1b) is known as the Sommerfeld radiation boundary condition. The PAL technique to be introduced is applicable to the Helmholtz problems with other types of boundary conditions such as Dirichlet or impendence boundary condition on Γ_D, and can also be used to solve acoustic wave propagations in inhomogeneous media in bounded domains.

We start with a general set-up for the star-shaped truncated domain and provide new perspectives of the circular PAL reported in [53], which sheds light on the study of general PAL with star-shaped domain truncation in the forthcoming section.

3.1. Star-shaped truncated domain. As illustrated in Figure 4, we enclose $\bar{D}$ by a star-shaped domain $\Omega_{\rm s}$ with respect to the origin. Assume that the boundary of $\Omega_{\rm s}$ is piecewise smooth with the parametric form in the polar coordinates, viz.,

$$\Gamma_{R_1} := \partial\Omega_{\rm s} = \big\{(r,\theta) \,:\, r = R_1(\theta), \ \ \theta \in [0, 2\pi)\big\}, \tag{3.2}$$

or equivalently, Γ_{R_1} has the parametric form in Cartesian coordinates:

$$\Gamma_{R_1} = \big\{\boldsymbol{x} = (x,y) \,:\, x = R_1(\theta)\cos\theta, \ y = R_1(\theta)\sin\theta, \ \theta \in [0, 2\pi)\big\}. \tag{3.3}$$

Then the artificial layer is formed by surrounding $\Omega_{\rm s}$ with

$$\Omega_\varrho^{\rm PAL} := \big\{(r,\theta) \,:\, R_1(\theta) < r < R_2(\theta) := \varrho R_1(\theta), \ \ \theta \in [0, 2\pi)\big\}, \tag{3.4}$$

where the constant $\varrho > 1$ can tune the "thickness" of the layer. The layer $\Omega_\varrho^{\rm PAL}$ provides a star-shaped domain truncation of the unbounded domain Ω_e. We further denote the domain of interest and the real computational domain, respectively, by

$$\Omega := \Omega_{\rm s} \setminus \bar{D}, \quad \Omega_{\rm c} := \Omega_\varrho^{\rm PAL} \cup \Omega \cup \Gamma_{R_1}, \tag{3.5}$$

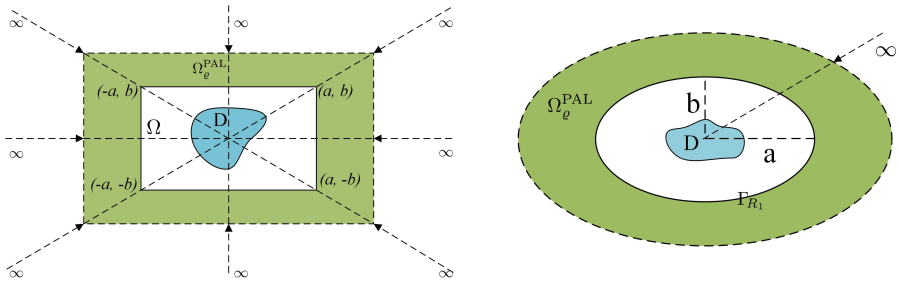

FIG. 4. *Schematic illustration of the artificial layers. Left: a rectangular PAL with four trapezoidal patches formed by compressing the open space exterior to the inside (unshaded) rectangular domain with the boundary* $r = R_1(\theta)$ *given by* (3.8) *into the shaded rectangular layer via the mapping* (3.11)–(3.12) *along the* r*-direction. Here, for a fixed angle* θ, $\tilde{r} = \infty$ *is mapped to* $r = \varrho R_1(\theta)$ *(cf.* (3.6)*). Right: an elliptical PAL formed by the compression of the open space exterior to the unshaded elliptical domain into the shaded elliptic layer via the mapping* (3.11)–(3.12).

where we need to approximate the original solution in Ω, but have to couple the original equation in Ω with the artificial equation in $\Omega_\varrho^{\rm PAL}$ in real computation.

Since the choice of the truncated domains is a priori arbitrary, it could be advantageous to choose nonclassical shapes to offer more flexibility to deal with non-standard geometry of the scatterer and inhomogeneity of the media. It is important to note that the configuration of the artificial layer is solely determined by the parametric form of $R_1(\theta)$ and the tuning "thickness" parameter ϱ. We list below some typical examples of such star-shaped domain truncation.

(i) In the circular case, the artificial layer is an annulus, i.e.,

$$\Omega_\varrho^{\rm PAL} = \{R_1 < r < R_2 = \varrho R_1,\ 0 \le \theta < 2\pi\}, \tag{3.6}$$

where R_1 is independent of θ. As a variant, the "perturbed" annular layer takes the form

$$\Omega_\varrho^{\rm PAL} = \{R_1(\theta) = a + b\sin\theta < r < R_2(\theta) = \varrho R_1(\theta),\ 0 \le \theta < 2\pi\}, \tag{3.7}$$

where $a > b > 0$ are some given constants.

(ii) In the rectangular case, we take, for instance, the boundary Γ_{R_1} as a square with four vertices: $(a,b), (-a,b), (-a,-b), (a,-b)$ with $a, b > 0$ (see Figure 4 (left)). Then we have

$$R_1(\theta) = \begin{cases} a\sec\theta, & \theta \in [0,\theta_0) \cup [2\pi - \theta_0, 2\pi), \\ b\csc\theta, & \theta \in [\theta_0, \pi - \theta_0), \\ -a\sec\theta, & \theta \in [\pi - \theta_0, \pi + \theta_0), \\ -b\csc\theta, & \theta \in [\pi + \theta_0, 2\pi - \theta_0), \end{cases} \qquad \theta_0 = \arctan\frac{b}{a}. \tag{3.8}$$

Similarly, we can consider a general rectangular domain truncation.

(iii) If we choose Γ_{R_1} to be an ellipse, $\frac{x^2}{a^2} + \frac{y^2}{b^2} = 1$ with $a > b > 0$ (see Figure 4 (right)), then we have

$$R_1(\theta) = \frac{ab}{\sqrt{b^2 + (a^2 - b^2)\sin^2\theta}}, \quad \theta \in [0, 2\pi). \tag{3.9}$$

Now, the key issue is how to construct the governing equation in the artificial layer. In practice, one wishes that (i) the solution of the resulted coupled problem in $\Omega_{\rm c}$ can approximate the original solution $U|_\Omega$ as accurately as possible to avoid the pollution of the truncation, but (ii) the layer $\Omega_\varrho^{\rm PAL}$ should be thin enough to save computational cost. To show the essence of designing the PAL-equation for the above general star-shaped truncated domain, we first recap on the circular PAL proposed in [53], but we explore this technique from a very different viewpoint.

3.2. Some new perspectives of the circular PAL. As some new insights, we next show that the governing equation (in the annular layer $r \in (R_1, R_2)$) in [53] can be obtained from the Bérenger equation (in the unbounded domain $\rho > R_1$; see Collino and Monk [16]) by a real compression transformation. Then we can claim the exactness of the PAL technique—the PAL-solution for $r < R_1$ coincides with the original solution $U|_{r<R_1}$. This should be in contrast with the PML technique [16, 10], where the governing equation in the layer is obtained by naively truncating the Bérenger equation in unbounded domain at $r = R_2$, and then imposing the homogeneous Dirichlet boundary condition.

Like (2.22), Zharova, Shadrivov, and Kivshar [57] introduced the real compression transformation

$$\rho := \rho(r) = R_1 + (R_2 - R_1)\frac{r - R_1}{R_2 - r} \quad \text{or} \quad r = R_2 - \frac{(R_2 - R_1)^2}{\rho + R_2 - 2R_1}, \tag{3.10}$$

for $\rho \in (R_1, \infty)$ and $r \in (R_1, R_2)$, to design the inside-out (or inverse) invisibility cloak and also a matched layer. In principle, it compresses all the infinite space $R_1 < \rho < \infty$ into the finite annulus $R_1 < r < R_2$, where ideally the wave propagation is expected to be equivalent to the wave propagation in the infinite space. However, such a technique fails to work, as the numerical approximation of the waves within the layer suffers from *the curse of infinite oscillation* [33].

Following [53], we propose to fill the cloaking layer with lossy media (i.e., complex material parameters) and deal with the singular media by using a suitable substitution of unknowns. More precisely, we introduce the compression complex coordinate transformation in polar coordinates:

$$\tilde r = S(r) = \begin{cases} r, & r < R_1, \\ R_1 + \sigma_1 T(r) + {\rm i}\,\sigma_0\, T(r), & R_1 < r < R_2, \end{cases} \qquad \tilde\theta = \theta, \quad \theta \in [0, 2\pi), \tag{3.11}$$

where $\sigma_0, \sigma_1 > 0$ are tuning parameters, and

$$T(r) = \frac{(R_2 - R_1)(r - R_1)}{R_2 - r} = (R_2 - R_1)^2 \int_{R_1}^{r} \frac{{\rm d}t}{(R_2 - t)^2}, \quad r \in (R_1, R_2). \tag{3.12}$$

It is noteworthy that $\Im\{\tilde r\}$ defines a compression mapping between $(0, \infty)$ and (R_1, R_2), and the parameters σ_0, σ_1 can be k-dependent, e.g., a constant multiple of $1/k$.

The PAL-equation can be obtained by applying the complex coordinate transformation (3.11) to the Helmholtz problem (3.1) in $(\tilde r, \tilde\theta)$-coordinates (see [53]),

$$\begin{cases} \dfrac{1}{r}\dfrac{\partial}{\partial r}\left(\dfrac{\beta r}{\alpha}\dfrac{\partial U_{\rm PAL}}{\partial r}\right) + \dfrac{1}{r^2}\dfrac{\alpha}{\beta}\dfrac{\partial^2 U_{\rm PAL}}{\partial \theta^2} + \alpha\beta\, k^2\, U_{\rm PAL} = f \quad \text{in } \Omega \cup \Omega_\varrho^{\rm PAL}, \\ U_{\rm PAL} = g \quad \text{on } \Gamma_D, \quad |U_{\rm PAL}| \text{ is uniformly bounded as } r \to R_2, \end{cases} \tag{3.13}$$

together with the usual transmission conditions at $\rho = R_1$. Here, we denoted

$$\alpha = \frac{d\tilde r}{dr}, \quad \beta = \frac{\tilde r}{r}. \tag{3.14}$$

3.2.1. Bérenger's equations and PML techniques. In [53], we adopted the transformed Sommerfeld radiation boundary condition as $r \to R_2$. In fact, it is only necessary to impose the uniform boundedness to guarantee the unique solvability and exactness with $U|_{r\le R_1} = U_{\rm p}|_{r\le R_1}$ (see Theorem 3.1 below). To justify this, we next show that the PAL-equation (3.13) can be derived from the Bérenger's equation (in unbounded domain) in [16]. Indeed, using separation of variables, the solution U of the Helmholtz problem (3.1) exterior to the circle $r = R_1$ can be written as

$$U(\boldsymbol{x}) = \sum_{|m|=0}^{\infty} a_m \frac{H_m^{(1)}(kr)}{H_m^{(1)}(kR_1)} e^{{\rm i}m\theta}, \quad r \ge R_1, \tag{3.15}$$

where $\boldsymbol{x} = re^{{\rm i}\theta}$, $H_m^{(1)}$ is the Hankel function of first kind and order m, and $\{a_m\}$ are the Fourier expansion coefficients of U at $r = R_1$. This series converges uniformly for $r \ge R_1$ (cf. [43]). According to [16], the Bérenger's idea to design PML in the cylindrical coordinates can be interpreted as stretching the solution (3.15) to the complex domain so that the waves become evanescent. Recall the asymptotic behavior of the Hankel function (cf. [1]):

$$|H_m^{(1)}(k\tilde{r})| \sim \left| \sqrt{\frac{2}{\pi k\tilde{r}}}\, e^{{\rm i}(k(\Re\{\tilde{r}\}+{\rm i}\Im\{\tilde{r}\})-\frac{1}{2}m\pi-\frac{1}{4}\pi)} \right| = \sqrt{\frac{2}{\pi k|\tilde{r}|}} e^{-k\Im\{\tilde{r}\}} \tag{3.16}$$

for $-\pi < \arg\{\tilde{r}\} < \pi$. This implies that the extension should be made in the upper half-plane such that $\Im\{\tilde{r}\} \to \infty$ as $|\tilde{r}| \to \infty$. In the PML technique, one uses the complex change of variables,

$$\tilde{r} = \tilde{r}(\rho) = \begin{cases} \rho & \text{for } \rho < R_1, \\ \rho + {\rm i}\displaystyle\int_{R_1}^{\rho} \hat{\sigma}(t){\rm d}t & \text{for } R_1 \le \rho < \infty, \end{cases} \tag{3.17}$$

where in general, the ABF $\hat{\sigma}$ satisfies

$$\hat{\sigma} \in C(\mathbb{R}), \quad \hat{\sigma} \ge 0 \quad \text{and} \quad \lim_{r\to\infty} \int_{R_1}^{r} \hat{\sigma}(t){\rm d}t = \infty. \tag{3.18}$$

Denote $\hat{\alpha} = \tilde{r}'(\rho)$ and $\hat{\beta} = \tilde{r}(\rho)/\rho$. Applying the coordinate transformation (3.17) to the Helmholtz equation exterior to the circle of radius R_1, we can obtain the Bérenger's problem of computing the Bérenger's solution $U_{\rm B}$ in the form (cf. [16])

$$\begin{cases} \dfrac{1}{\rho}\dfrac{\partial}{\partial\rho}\left(\dfrac{\hat{\beta}\rho}{\hat{\alpha}}\dfrac{\partial U_{\rm B}}{\partial\rho}\right) + \dfrac{1}{\rho^2}\dfrac{\hat{\alpha}}{\hat{\beta}}\dfrac{\partial^2 U_{\rm B}}{\partial\theta^2} + \hat{\alpha}\hat{\beta}\,k^2\,U_{\rm B} = f \quad \text{in } \Omega_e = \mathbb{R}^2 \setminus \bar{D}, \\ U_{\rm B} = g \quad \text{on } \Gamma_D, \\ |U_{\rm B}| \ \text{ is uniformly bounded as } \rho \to \infty\,, \end{cases} \tag{3.19}$$

together with the usual transmission conditions at $\rho = R_1$. Note that $\hat{\alpha} = \hat{\beta} = 1$ for $|\boldsymbol{x}| \le R_1$. According to [16, Theorem 1], the problem (3.19) admits a unique solution, and for any $|\boldsymbol{x}| \ge R_1$, the Bérenger's solution takes the form

$$U_{\rm B}(\boldsymbol{x}) = \sum_{|m|=0}^{\infty} a_m \frac{H_m^{(1)}(k\tilde{r}(\rho))}{H_m^{(1)}(kR_1)} e^{{\rm i}m\theta}, \tag{3.20}$$

where $\{a_m\}$ are the same as in (3.15). In other words, *the Bérenger's solution coincides with the solution of the original problem* (3.1) *for* $r < R_1$.

As shown in [16, 10], the PML technique directly truncates (3.19) at $\rho = R_2$, and the homogeneous boundary condition $U_{\rm PML} = 0$ at $\rho = R_2$ is then imposed. More precisely, we have the following PML-equation:

(3.21)
$$\begin{cases} \dfrac{1}{r}\dfrac{\partial}{\partial r}\left(\dfrac{\hat\beta r}{\hat\alpha}\dfrac{\partial U_{\rm PML}}{\partial r}\right) + \dfrac{1}{r^2}\dfrac{\hat\alpha}{\hat\beta}\dfrac{\partial^2 U_{\rm PML}}{\partial\theta^2} + \hat\alpha\hat\beta\, k^2\, U_{\rm PML} = f \quad \text{in } \Omega_e \cap \{|\boldsymbol{x}| < R_2\}, \\ U_{\rm PML}\big|_{\Gamma_D} = g\,; \quad U_{\rm PML}\big|_{r=R_2} = 0, \end{cases}$$

where we set $r = \rho$ as the independent variable for clarity. Like the waveguide setting in (2.14)–(2.15), the following two types of ABFs have been used in practice.

(i) PML$_n$ with bounded (or regular) ABFs (see, e.g., [16, 10]):

$$\hat\sigma(t) = \sigma_0\left(\frac{t - R_1}{R_2 - R_1}\right)^n, \quad \text{so} \quad \tilde r = r + \mathrm{i}\,\sigma_0\,\frac{R_2 - R_1}{n+1}\left(\frac{r - R_1}{R_2 - R_1}\right)^{n+1}, \tag{3.22}$$

where $r \in (R_1, R_2)$ and n is a positive integer. We refer to [10] for the detailed error analysis and also the very recent work [36] for insightful wavenumber explicit error estimates.

(ii) PML$_\infty$ with unbounded (or singular) ABFs (see [7, 8]):

$$\hat\sigma(t) = \frac{\sigma_0}{R_2 - t}, \quad \text{so} \quad \tilde r = r + \mathrm{i}\,\sigma_0\,\ln\left(\frac{R_2 - R_1}{R_2 - r}\right), \quad r \in (R_1, R_2). \tag{3.23}$$

Compared with the PML$_n$, the PML$_\infty$ renders the solution decay at an infinite rate near the outer boundary $r = R_2$. The parameter σ_0 plays a less important role than that for a bounded ABF. In fact, this technique was claimed to be "parameter-free" in [15] (where σ_0 was fixed in the numerical tests). However, it is noteworthy that the coefficients $\hat\alpha = \tilde r'(r)$ and $\hat\beta = \tilde r(r)/r$ in (3.21) are singular at $r = R_2$, which bring about some numerical difficulties for high wavenumbers and thin layers.

3.2.2. Equivalence of Bérenger's problem and PAL-equation. We next show that our proposed PAL-equation exactly solves the transformed problem (3.19) by further transforming it to a bounded domain by using a real compression mapping.

THEOREM 3.1. *Let* $U_{\rm B}(\rho, \theta)$ *be the solution of the Bérenger's problem* (3.19) *with* $\hat\sigma = \sigma_0/\sigma_1$ *in* (3.17)*, that is, the complex coordinate transformation:*

$$\tilde r = \rho + \mathrm{i}\frac{\sigma_0}{\sigma_1}(\rho - R_1) \quad \text{for } \rho > R_1. \tag{3.24}$$

Then applying the real compression rational mapping

$$\rho = R_1 + \sigma_1 T(r) = R_1 + \sigma_1\frac{(R_2 - R_1)(r - R_1)}{R_2 - r} \tag{3.25}$$

to (3.17)*, we can derive the circular PAL-equation* (3.13)*. Moreover, the PAL-equation* (3.13) *admits a unique solution, and*

$$U_{\rm PAL}(r, \theta) = U_{\rm B}\big(R_1 + \sigma_1 T(r), \theta\big), \quad r < R_2; \quad \text{and} \quad U_{\rm PAL}|_{r<R_1} = U|_{r<R_1}, \tag{3.26}$$

where U *is the solution of the original problem* (3.1)*.*

Proof. It suffices to consider the transformation for $\rho > R_1$. We find from (3.17) with $\hat{\sigma} = \sigma_0/\sigma_1$ that $\hat{\alpha} = 1+\mathrm{i}\sigma_0/\sigma_1$ and $\hat{\beta} = (\rho+\mathrm{i}\sigma_0(\rho-R_1)/\sigma_1)/\rho$. Using the rational mapping $\rho = R_1 + \sigma_1 T(r)$, we obtain from (3.14) and the composite transformation (3.24)–(3.25) (i.e., (3.11)) that

$$\begin{aligned} \alpha &= (\sigma_1 + \mathrm{i}\sigma_0)T'(r) = \hat{\alpha}\,\frac{d\rho}{dr}, \\ \beta &= \frac{R_1 + (1+\mathrm{i}\sigma_0)T(r)}{r} = \frac{\rho + \mathrm{i}\sigma_0(\rho - R_1)}{\rho} = \hat{\beta}\frac{\rho}{r}. \end{aligned} \tag{3.27}$$

By a simple substitution, $\frac{d}{d\rho} = \frac{dr}{d\rho}\frac{d}{dr}$, we can obtain (3.27) from (3.19) straightforwardly.

The unique solvability of (3.13) follows directly from that of (3.19) (see [16, Theorem 1]). Moreover, the PAL-solution is a compression of the Bénenger solution, $U_{\mathrm{p}}(r,\theta) = U_{\mathrm{B}}(R_1 + \sigma_1 T(r), \theta)$ for $r < R_2$, so it is identical to the original solution for $r < R_1$. Thus, by (3.20), we have

$$U_{\mathrm{p}}(\boldsymbol{x}) = \sum_{|m|=0}^{\infty} \hat{a}_m \,\frac{H_m^{(1)}(kS(r))}{H_m^{(1)}(kR_1)} e^{\mathrm{i}m\theta}, \quad R_1 < r < R_2, \tag{3.28}$$

where $\{\hat{a}_m\}$ are the Fourier coefficients of $U_{\mathrm{p}}(R_1,\theta)$. ∎

With the above understanding, we can show that the PAL-solution in the artificial layer decays exponentially. In fact, the bound is more precise than the estimate in [53, Theorem 1].

THEOREM 3.2. *The solution of the PAL-equation* (3.13) *satisfies that for all* $r \in [R_1, R_2)$,

$$\int_0^{2\pi} |U_{\mathrm{PAL}}(r,\theta)|^2 d\theta \le \exp\left(-\sigma_0 k \frac{\tau}{1-\tau}\big(1 - h(\tau)(1-\tau)^2\big)^{1/2}\right) \int_0^{2\pi} |U_{\mathrm{PAL}}(R_1,\theta)|^2 d\theta,$$

where

$$h(\tau) = \frac{R_1^2}{(R_1(1-\tau) + \sigma_1 d\,\tau)^2 + \sigma_0^2 d^2\,\tau^2}, \quad d = R_2 - R_1, \quad \tau = \frac{r - R_1}{R_2 - R_1} \in [0,1).$$

Proof. We now show that the PAL-solution decays exponentially in the PAL layer. For this purpose, we recall the uniform estimate of Hankel functions first derived in [10, Lemma 2.2]: *For any complex* z *with* $\Re\{z\}, \Im\{z\} \ge 0$, *and for any real* Θ *such that* $0 < \Theta \le |z|$, *we have*

$$|H_\nu^{(1)}(z)| \le e^{-\Im\{z\}\left(1 - \frac{\Theta^2}{|z|^2}\right)^{1/2}} |H_\nu^{(1)}(\Theta)|, \tag{3.29}$$

which is valid for any real order ν. Note that $S(R_1) = R_1$, and for $r \in [R_1, R_2)$,

$$|S(r)|^2 = (R_1 + \sigma_1 T(r))^2 + \sigma_0^2 T^2(r) \ge R_1^2\,, \quad \Im\{S(r)\} = \sigma_0 T(r).$$

Thus, we obtain from (3.29) with $z = kS(r)$ and $\Theta = kR_1$ that for $r \in [R_1, R_2)$,

$$\begin{aligned} \max_{|m|\ge 0} \left|\frac{H_m^{(1)}(kS(r))}{H_m^{(1)}(kR_1)}\right| &\le \exp\left\{-k\Im\{S(r)\}\left(1 - \frac{R_1^2}{|S(r)|^2}\right)^{1/2}\right\} \\ &= \exp\left(-\sigma_0 dk \frac{\tau}{1-\tau}\big(1 - h(\tau)(1-\tau)^2\big)^{1/2}\right), \end{aligned} \tag{3.30}$$

where the last step follows from direct calculation. ∎

It is seen that the PAL-equation leads to the exact Bérenger solution, which decays exponentially to zero at a rate $O(e^{-\sigma_0 dk/(1-\tau)})$ as $r \to R_2$ (i.e., as $\tau \to 1$). However, there are two numerical issues to be addressed.

(i) The coefficients of the PAL-equation (3.21) are singular, which are induced by the compression rational mapping $\rho = R_1 + \sigma_1 T(r)$. In fact, we have

$$\alpha(r) \sim \frac{C_1}{(R_2 - r)^2}, \quad \beta(r) \sim \frac{C_2}{R_2 - r}.$$

However, the underlying PAL-solution is not singular at $r = R_2$, as it decays exponentially in the artificial layer.

(ii) Observe from (3.16) that the real part of the transformation $\rho = \Re\{S(r)\} = R_1 + \sigma_1 T(r)$ may increase the oscillation near the inner boundary $r = R_1$.

To resolve these two issues, we follow [53] by using a substitution of the unknown $U_{\rm PAL} = w(r)V_{\rm p}$ with a suitable factor $w(r)$, so that V_p to be approximated is well-behaved. The choice of w is spawned by the asymptotic behavior due to (3.16):

$$\begin{aligned} \frac{H_m^{(1)}(kS(r))}{H_m^{(1)}(kR_1)} &\sim \sqrt{\frac{R_1}{S(r)}}\, e^{{\rm i}k(\Re\{S(r)\}-R_1)} e^{-k\Im\{S(r)\}} \\ &= \sqrt{\frac{R_1}{S(r)}}\, e^{{\rm i}k\sigma_1 T(r)} e^{-k\Im\{S(r)\}}. \end{aligned} \tag{3.31}$$

It implies the oscillatory part of $U_{\rm PAL}$ can be extracted explicitly: $U_{\rm PAL}(r,\theta) = e^{{\rm i}k\sigma_1 T(r)} \widetilde{U}_{\rm PAL}(r,\theta)$, where $\widetilde{U}_{\rm p}(r,\theta)$ is expected to have no essential oscillation. Then the second issue can be resolved effectively. In regard to the first issue, it is seen from Theorem 3.1 that the singular coefficients are induced by the real transformation: $\rho = R_1 + \sigma_1 T(r)$. In fact, similar singular mapping techniques were used to map elliptic problems with rapid decaying solutions in unbounded domains to problems with singular coefficients in bounded domains (see, e.g., [9, 29, 48, 47] and the references therein), so one can also consider a suitable variational formulation weighted with $\omega(r) = R_2 - r$. Unfortunately, the involved variational formulation is nonsymmetric and less efficient in computation. As shown in [53], we can absorb the singularity and diminish the oscillation by the substitution

$$U_{\rm p}(r,\theta) = w(r) V_{\rm p}(r,\theta), \quad r < R_2, \tag{3.32}$$

where

$$w(r) = \begin{cases} 1 & \text{for } r < R_1, \\ \big(R_1/(R_1 + \sigma_1 T(r))\big)^{3/2} e^{{\rm i}k\sigma_1 T(r)} & \text{for } R_1 \le r < R_2, \end{cases} \tag{3.33}$$

which leads to a well-behaved and nonoscillatory field $V_{\rm p}$ in the absorbing layer. It will be clear from Theorem 4.5 that the fractional power 3/2 is the lowest that can eliminate the singular factors in the coefficients of the Galerkin formulation of $V_{\rm p}$.

It is important to remark that in numerical discretization, we can build the substitution in the basis functions. More precisely, we approximate $U_{\rm PAL}$ by the nonstandard basis $\{w\phi_k\}$ (where $\{\phi_k\}$ are usual spectral or finite element basis functions) to avoid transforming the PAL-equation into a much more complicated problem in $V_{\rm p}$. In the above, we just show the idea, but refer to [53] and the more general case in section 4 for the detailed implementation.

4. The PAL technique for star-shaped domain truncation. With the understanding of the circular case, we are now in a position to construct the PAL technique for the general star-shaped domain truncation with the setting described in subsection 3.1. We start with constructing the PAL-equation based on the complex compression coordinate transformation. Then we show the outstanding performance of this technique.

4.1. Design of the PAL-equation. The first step is to extend the complex compression coordinate transformation (3.11) to the general case:

$$\tilde{r} = S(r,\theta) = \begin{cases} r & \text{in } \Omega, \\ R_1(\theta) + \sigma_1\, T(r,\theta) + \mathrm{i}\,\sigma_0\, T(r,\theta) & \text{in } \Omega_\varrho^{\mathrm{PAL}}, \end{cases} \quad \tilde{\theta} = \theta,\ \theta \in [0, 2\pi), \tag{4.1}$$

where

$$T(r,\theta) = \frac{(R_2 - R_1)(r - R_1)}{R_2 - r} = (R_2 - R_1)^2 \int_{R_1}^{r} \frac{\mathrm{d}t}{(R_2 - t)^2}, \quad r \in (R_1, R_2). \tag{4.2}$$

Different from the circular case, R_1 and R_2 are now θ-dependent. Indeed, we notice from (3.2) and (3.4) that $R_1 = R_1(\theta)$ defines the inner boundary of the artificial layer $\Omega_\varrho^{\mathrm{PAL}}$, whose outer boundary is given by $R_2 = \varrho R_1(\theta)$. For any fixed $\theta \in [0, 2\pi)$, $\Re\{\tilde{r}\} = R_1(\theta) + \sigma_1\, T(r,\theta)$ compresses the infinite "ray" $R_1 \to \infty$ into a "line segment" $R_1 \to R_2$ in the radial direction. Accordingly, for all $\theta \in [0, 2\pi)$, it compresses the open space exterior to the star-shaped domain $\{r < R_1\}$ to the artificial layer $\Omega_\varrho^{\mathrm{PAL}}$ (see Figure 4 for an illustration).

Remark 4.1. Based on the notion of transformation optics [41], the use of a real singular coordinate transformation to expand the origin into a polygonal or star-shaped domain to design invisibility cloaks is discussed in, e.g., [56, 54]. In contrast, the real part of the transformation (4.1) $R_1(\theta) + \sigma_1\, T(r,\theta)$ compresses the infinity to the finite boundary $r = R_2(\theta)$, so the cloaking is an inside-out or inverse cloaking as with [57]. However, to the best of our knowledge, this type of cloaking has not been studied in the literature.

In order to derive the PAL-equation in Cartesian coordinates, it is necessary to commute between different coordinates in the course as shown in the diagram

$$\boxed{\text{Cartesian: } (\tilde{x}, \tilde{y})} \longleftrightarrow \boxed{\text{Polar: } (\tilde{r}, \tilde{\theta})} \xrightarrow{\text{Transform}} \boxed{\text{Polar: } (r, \theta)} \longleftrightarrow \boxed{\text{PAL: } (x, y)}$$

In what follows, the differential operators "$\nabla, \nabla\cdot$" are in (x, y)-coordinates, but the coefficient matrix $\boldsymbol{C}$ and the reflective index n are expressed in (r, θ)-coordinates. For simplicity, we denote the partial derivatives by $S_r = \partial_r S$ and $S_\theta = \partial_\theta S$, etc.

The most important step is to obtain the transformed Helmholtz operator as follows, whose derivation is given in Appendix B.

LEMMA 4.2. *Using the transformation* (4.1)*, the Helmholtz operator*

$$\tilde{\mathcal{H}}[\tilde{U}] := \Delta \tilde{U} + k^2 \tilde{U}, \tag{4.3}$$

in $(\tilde{x}, \tilde{y})$*-coordinates, can be transformed into*

$$\mathcal{H}[U_{\mathrm{p}}] := \frac{1}{n}\big\{\nabla \cdot \big(\boldsymbol{C}\, \nabla U_{\mathrm{p}}\big) + k^2\, n\, U_{\mathrm{p}}\big\}, \tag{4.4}$$

where $U_{\rm p}(x,y)=\tilde{U}(\tilde{x},\tilde{y})$, $\boldsymbol{C}=(C_{ij})$ *is a two-by-two symmetric matrix, and* n *is the reflective index given by*

$$\boldsymbol{C}=\boldsymbol{T}\,\boldsymbol{B}\,\boldsymbol{T}^t,\quad n=\frac{SS_r}{r}, \tag{4.5}$$

and

$$\boldsymbol{B}=\begin{pmatrix}\dfrac{S}{rS_r}\left(1+\dfrac{S_\theta^2}{S^2}\right) & -\dfrac{S_\theta}{S}\\ -\dfrac{S_\theta}{S} & \dfrac{rS_r}{S}\end{pmatrix},\qquad \boldsymbol{T}=\begin{pmatrix}\cos\theta & -\sin\theta\\ \sin\theta & \cos\theta\end{pmatrix}. \tag{4.6}$$

With the aid of Lemma 4.2, we directly apply (4.1)–(4.2) to the exterior Helmholtz problem and obtain the PAL-equation for the general star-shaped truncation of the unbounded domain.

THEOREM 4.3. *The PAL-equation associated with star-shaped domain truncation of the original Helmholtz problem* (3.1) *takes the form*

$$\begin{cases}\nabla\cdot\big(\boldsymbol{C}\,\nabla U_{\rm PAL}\big)+k^2\,n\,U_{\rm PAL}=f \quad \text{in } \ \Omega\cup\Omega_\varrho^{\rm PAL},\\ U_{\rm PAL}=g \quad \text{on } \ \Gamma_D,\\ |U_{\rm PAL}| \ \textit{is uniformly bounded as } r\to R_2\,,\end{cases} \tag{4.7}$$

where $\boldsymbol{C}=\boldsymbol{I}, n=1$ *in* Ω, *and* $\boldsymbol{C}, n$ *in* $\Omega_\varrho^{\rm PAL}$ *are the same as in Lemma* 4.2 *with the transformation* S *given by* (4.1)–(4.2). *Here, we impose the usual transmission conditions across the interface* $\Gamma_{R_1}: r=R_1$.

As an extension of the circular case, the asymptotic boundary condition at $r=R_2$ is derived from the transformed Sommerfeld radiation condition and rapid decay of $U_{\rm PAL}$ near the outer boundary of the artificial layer $\Omega_\varrho^{\rm PAL}$. Moreover, we can extend (3.24) to the θ-dependent situation, $\tilde{r}=\rho$ for $\rho<R_1$, and

$$\tilde{r}=\tilde{r}(\rho,\theta)=\rho+{\rm i}\frac{\sigma_1}{\sigma_0}\big(\rho-R_1(\theta)\big)\qquad \text{for}\quad \rho>R_1, \tag{4.8}$$

and then apply Lemma 4.2 to derive the Bérenger-type problem in the unbounded domain like (3.19). To understand the oscillatory behavior of the underlying solution, we recall the Karp's "farfield" expansion (cf. [34, Theorem I]): the solution of the Helmholtz equation $\Delta u+k^2u=0$ exterior to a circle of radius a has an expansion

$$u(\rho,\theta)=H_0^{(1)}(k\rho)\sum_{l=0}^{\infty}\frac{F_l(\theta)}{(k\rho)^l}+H_1^{(1)}(k\rho)\sum_{l=0}^{\infty}\frac{G_l(\theta)}{(k\rho)^l},$$

which converges uniformly and absolutely for $\rho\ge b>a$, and can be differentiated termwise with respect to ρ. As the compression is along the radial ρ-direction, we fix $\theta=\theta^*$ and let $a\ge R_1(\theta_*)$ be the radius of the circle enclosing the scatterer D and all the inhomogeneity. By (3.16) with $m=0,1$, the essential oscillation of $u(\tilde{r},\theta^*)$ is of the form $e^{{\rm i}k\Re\{\tilde{r}\}}=e^{{\rm i}k\rho}$. Note that the PAL transformation (4.1) is a composition of (4.8) and the real compression transformation: $\rho=R_1+\sigma_1T(r,\theta^*)$ (along the ray $\theta=\theta^*$). As a result, we introduce the substitution in (4.11) below, where a factor is normalized to ensure the continuity of the fields across the interface $r=R_1$ as $T(R_1,\theta_*)=0$.

4.2. Substitution and implementation. A key to success of the PAL technique is to make a substitution of the unknown that can deal with the singular coefficients at $r = R_2$ and diminish the oscillation near $r = R_1$. To fix the idea, we assume that $g = 0$ and define the space

$$H^1_{0,\Gamma}(\Omega_{\rm c}) = \big\{\phi \in H^1(\Omega_{\rm c}) : \phi\,|_\Gamma = 0\big\}, \quad \Gamma := \partial D, \tag{4.9}$$

and

$$\Omega_{\rm c} := \Omega \cup \Omega^{\rm PAL}_\varrho \cup \big\{r = R_1(\theta) :\ \theta \in [0, 2\pi)\big\}.$$

A weak form of (4.7) is to find $u = wv$ with $v \in H^1_{0,\Gamma}(\Omega_{\rm c})$ such that

$$\mathscr{B}(u,\psi) = (\boldsymbol{C}\,\nabla u, \nabla\psi)_{\Omega_{\rm c}} - k^2(n\,u,\psi)_{\Omega_{\rm c}} = (f,\phi)_\Omega \tag{4.10}$$

for all $\psi = w\,\phi$ with $\phi \in H^1_{0,\Gamma}(\Omega_{\rm c})$, where

$$w\,|_\Omega = 1, \quad w\,|_{\Omega^{\rm PAL}_\varrho} = t^{3/2}\,e^{{\rm i}k\sigma_1 T(r,\theta)}, \quad t := \frac{R_1}{\Re\{S\}} = \frac{R_1}{R_1 + \sigma_1 T}. \tag{4.11}$$

Recall that the source term $f(x)$ is compactly supported in Ω where $w = 1$, so we have the nonweighted L^2-inner product $(f,\phi)_\Omega$. Note that we extract the above oscillatory component, together with the singular factor $t^{3/2}$, to form w. As we shall see later on, the power $3/2$ is the smallest to absorb all singular factors. On the other hand, in numerical approximation, we approximate v by standard spectral-element and finite-element methods, so it is necessary to compute the associated "stiffness" matrix: $\mathscr{B}(wv, w\phi)$ with v, ϕ being in the solution and test function spaces.

We next provide a detailed representation of the transformed sesquilinear form for the convenience of both the computation and also the analysis of the problem in v. For clarity, we reformulate (4.10) as follows: find $v \in H^1_{0,\Gamma}(\Omega_{\rm c})$ (and set $u = w\,v$) such that

$$\breve{\mathscr{B}}(v,\phi) := \mathscr{B}(wv, w\phi) = (\boldsymbol{C}\,\nabla(wv), \nabla(w\,\phi))_{\Omega_{\rm c}} - k^2(n\,|w|^2 v, \phi)_{\Omega_{\rm c}} = (f,\phi)_\Omega \tag{4.12}$$

for all $\phi \in H^1_{0,\Gamma}(\Omega_{\rm c})$.

The following formulation holds for general differentiable w, which will be specified later for clarity of presentation.

LEMMA 4.4. *The sesquilinear form $\breve{\mathscr{B}}(v,\phi)$ in* (4.12) *can be rewritten as*

$$\begin{aligned}\breve{\mathscr{B}}(v,\phi) &= \big(|w|^2\boldsymbol{B}\breve{\nabla}v, \breve{\nabla}\phi\big)_{\Omega_{\rm c}} + \big(w\boldsymbol{B}\breve{\nabla}w^*\cdot\breve{\nabla}v, \phi\big)_{\Omega_{\rm c}} \\ &\quad + \big(w^*\boldsymbol{B}\breve{\nabla}w\,v, \breve{\nabla}\phi\big)_{\Omega_{\rm c}} + \big(\breve{n}v, \phi\big)_{\Omega_{\rm c}} \\ &= \big(\breve{\boldsymbol{B}}\breve{\nabla}v, \breve{\nabla}\phi\big)_{\Omega_{\rm c}} + \big(\boldsymbol{p}\cdot\breve{\nabla}v, \phi\big)_{\Omega_{\rm c}} + \big(v, \boldsymbol{q}^*\cdot\breve{\nabla}\phi\big)_{\Omega_{\rm c}} + \big(\breve{n}\,v, \phi\big)_{\Omega_{\rm c}},\end{aligned} \tag{4.13}$$

where $\breve{\nabla} = (\partial_r, \partial_\theta/r)^t$, *and*

$$\begin{aligned}&\breve{\boldsymbol{B}} := |w|^2\boldsymbol{B}, \quad \boldsymbol{p} := w\boldsymbol{B}\breve{\nabla}w^*, \\ &\boldsymbol{q} := w^*\boldsymbol{B}\breve{\nabla}w, \quad \breve{n} := (\breve{\nabla}w^*)^t\boldsymbol{B}\,\breve{\nabla}w - k^2\,|w|^2\,n,\end{aligned} \tag{4.14}$$

with $\boldsymbol{B}$ *and* n *defined in* (4.6). *In* (4.13), $\boldsymbol{B} = \breve{\boldsymbol{B}} = \boldsymbol{I}, \boldsymbol{p} = \boldsymbol{q} = \boldsymbol{0}$, *and* $n = -k^2$ *in* Ω.

Proof. One verifies readily that

$$\nabla = (\partial_x, \partial_y)^t = \boldsymbol{T}(\partial_r, \partial_\theta/r)^t = \boldsymbol{T}\,\breve{\nabla}. \tag{4.15}$$

For clarity, we denote $\xi = wv$ and $\eta = (w\,\phi)^*$. From (4.15), we immediately derive

$$(\nabla\eta)^t\boldsymbol{C}\nabla\xi = (\boldsymbol{T}\breve{\nabla}\eta)^t\,\boldsymbol{C}\,(\boldsymbol{T}\breve{\nabla}\xi) = (\breve{\nabla}\eta)^t\,(\boldsymbol{T}^t\boldsymbol{C}\boldsymbol{T})\,\breve{\nabla}\xi = \breve{\nabla}^t\eta\,\boldsymbol{B}\,\breve{\nabla}\xi, \tag{4.16}$$

where we used the fact $\boldsymbol{B} = \boldsymbol{T}^t\boldsymbol{C}\boldsymbol{T}$, due to (4.5), and the property $\boldsymbol{T}^{-1} = \boldsymbol{T}^t$. Since

$$\breve{\nabla}\xi = (\breve{\nabla}w)v + w\breve{\nabla}v, \quad \breve{\nabla}^t\eta = (\breve{\nabla}^t w^*)\phi^* + w^*\breve{\nabla}^t\phi^*, \tag{4.17}$$

we have

$$\begin{aligned}\big(\boldsymbol{C}\,\nabla(wv),\nabla(w\,\phi)\big)_{\Omega_c} &= \big(|w|^2\boldsymbol{B}\breve{\nabla}v,\breve{\nabla}\phi\big)_{\Omega_c} + \big(w\boldsymbol{B}\breve{\nabla}v,(\breve{\nabla}w)\phi\big)_{\Omega_c}\\ &\quad + \big(\boldsymbol{B}\breve{\nabla}w\,v,w\breve{\nabla}\phi\big)_{\Omega_c} + \big((\breve{\nabla}w^*)^t\boldsymbol{B}\breve{\nabla}w\,v,\phi\big)_{\Omega_c}.\end{aligned} \tag{4.18}$$

Thus, the representation (4.13) follows from (4.12) and (4.18). ∎

We next evaluate the terms involving $\boldsymbol{B}, n$, and w and show that the singular coefficients in (4.14) can be fully absorbed by w. Although the derivation appears a bit lengthy and tedious, we strive to present the formulation in an accessible manner, which depends only on the configuration of the layer: $R_1(\theta), \varrho$, and the coordinate transformation T and σ_0, σ_1. To make the derivation concise, we also express them in terms of

$$t = \frac{R_1}{R_1 + \sigma_1 T} = \frac{R_1(R_2 - r)}{R_1(R_2 - r) + \sigma_1(\varrho - 1)R_1(r - R_1)} \in (0, 1] \tag{4.19}$$

and use following regular functions in r:

$$\begin{aligned}&\alpha = \sigma_1 + \mathrm{i}\sigma_0, \quad \beta := tS = R_1 + (\alpha - \sigma_1)\tau,\\ &\tau := tT = \frac{(\varrho - 1)R_1^2(r - R_1)}{R_1(R_2 - r) + \sigma_1(\varrho - 1)R_1(r - R_1)},\\ &\gamma_1 := t^2T_r = \frac{(\varrho - 1)^2R_1^4}{(R_1(R_2 - r) + \sigma_1(\varrho - 1)R_1(r - R_1))^2},\\ &\gamma_2 := t^2T_\theta = (1 - \varrho)R_1^2R_1'\frac{R_1(R_2 - r) + r(r - R_1)}{(R_1(R_2 - r) + \sigma_1(\varrho - 1)R_1(r - R_1))^2},\end{aligned} \tag{4.20}$$

where we used

$$T_r = \left(\frac{(\varrho - 1)R_1}{R_2 - r}\right)^2, \quad T_\theta = (1 - \varrho)R_1'\frac{R_1(R_2 - r) + r(r - R_1)}{(R_2 - r)^2}. \tag{4.21}$$

With the following formulation in Cartesian coordinates at our disposal, the implementation of the PAL technique using the spectral and finite elements becomes a normal coding exercise.

THEOREM 4.5. *The sesquilinear form $\breve{\mathscr{B}}(v,\phi)$ takes the form*

$$\breve{\mathscr{B}}(v,\phi) = \big(\boldsymbol{T}\breve{\boldsymbol{B}}\boldsymbol{T}^t\,\nabla v,\nabla\phi\big)_{\Omega_c} + (\boldsymbol{T}\boldsymbol{p}\cdot\nabla v,\phi)_{\Omega_c} + (v,\boldsymbol{T}\boldsymbol{q}^*\cdot\nabla\phi)_{\Omega_c} + (\breve{n}\,v,\phi)_{\Omega_c}, \tag{4.22}$$

where the matrix $\boldsymbol{T}$ *is given in* (4.6). *In* Ω, *we have* $\breve{\boldsymbol{B}} = \boldsymbol{I}, \boldsymbol{p} = \boldsymbol{q} = \boldsymbol{0}$, *and* $n = -k^2$, *while in* $\Omega_\varrho^{\mathrm{PAL}}$, *the scalar function* $\breve{n}$, *and the entries of the matrix* $\breve{\boldsymbol{B}}$, *and the vectors* $\boldsymbol{p}, \boldsymbol{q}$ *in* (4.14) *can be evaluated by the following expressions:*

$$\breve{n} = k^2 \left(\frac{\beta\sigma_1^2}{\alpha} - \alpha\beta + \frac{\sigma_1^2 R_1'^2 t^2}{\alpha\beta} \right) \frac{\gamma_1}{r} + \frac{9\gamma_1\sigma_1^2 t^2}{4rR_1^2} \left(\frac{\beta}{\alpha} + \frac{R_1'^2}{\alpha\beta R_1^2} (R_1 t + \alpha\tau)^2 \right), \tag{4.23}$$

$$\begin{aligned} \breve{B}_{11} &= \frac{\beta t^2}{\alpha\gamma_1 r} \big(t^2 + (R_1' t^2 + \alpha\gamma_2)^2 \beta^{-2} \big), \\ \breve{B}_{12} &= -\big(R_1' t^2 + \alpha\gamma_2 \big) \frac{t^2}{\beta}, \quad \breve{B}_{22} = \frac{\alpha\gamma_1 r}{\beta} t^2, \end{aligned} \tag{4.24}$$

(4.25a)

$$p_1 = -\frac{\beta\sigma_1}{\alpha r} \left(\frac{3t}{2R_1} + \mathrm{i}k \right) t^2 - \left\{ \frac{3R_1'\sigma_1}{2rR_1\alpha\beta} \left(t + \frac{\alpha\tau}{R_1} \right) + \frac{\mathrm{i}k\sigma_1 R_1'}{r\alpha\beta} \right\} (R_1' t^2 + \alpha\gamma_2) t^2,$$

(4.25b)

$$p_2 = \frac{3R_1'\gamma_1\sigma_1}{2R_1\beta} \left(t + \frac{\alpha\tau}{R_1} \right) t^2 + \mathrm{i}k\sigma_1 \frac{R_1'\gamma_1}{\beta} t^2,$$

and the elements of $\boldsymbol{q}$ *can be obtained by changing the signs in front of* $\mathrm{i}k$ *in* p_1 *and* p_2, *i.e.,* $-\mathrm{i}k$ *in place of* $\mathrm{i}k$ *in* (4.25).

Proof. Using (4.15) and the property $\boldsymbol{T}^{-1} = \boldsymbol{T}$, we have $\breve{\nabla} = \boldsymbol{T}^t \nabla$. Accordingly, we can rewrite the formulation of $\breve{\mathscr{B}}(v, \phi)$ in Lemma 4.4 as

$$\begin{aligned} \breve{\mathscr{B}}(v, \phi) &= \big(\breve{\boldsymbol{B}} \breve{\nabla} v, \breve{\nabla} \phi \big)_{\Omega_c} + \big(\boldsymbol{p} \cdot \breve{\nabla} v, \phi \big)_{\Omega_c} + \big(v, \boldsymbol{q}^* \cdot \breve{\nabla} \phi \big)_{\Omega_c} + \big(\breve{n}\, v, \phi \big)_{\Omega_c} \\ &= (\boldsymbol{T} \breve{\boldsymbol{B}} \boldsymbol{T}^t \nabla v, \nabla \phi)_{\Omega_c} + (\boldsymbol{T}\boldsymbol{p} \cdot \nabla v, \phi)_{\Omega_c} \\ &\quad + (v, \boldsymbol{T}\boldsymbol{q}^* \cdot \nabla \phi)_{\Omega_c} + (\breve{n}\, v, \phi)_{\Omega_c}. \end{aligned} \tag{4.26}$$

Now, the main task is to derive the representations in (4.23)–(4.25). For clarity, we deal with them separately in three cases below.

(i) We first derive (4.23) from the expression in (4.14). By direct calculation, we find

$$\begin{aligned} (\breve{\nabla} w^*)^t \boldsymbol{B}\, \breve{\nabla} w &= (w_r^*, w_\theta^*/r) \begin{pmatrix} B_{11} & B_{12} \\ B_{12} & B_{22} \end{pmatrix} \begin{pmatrix} w_r \\ w_\theta/r \end{pmatrix} \\ &= B_{11} |w_r|^2 + \frac{B_{22}}{r^2} |w_\theta|^2 + \frac{B_{12}}{r} (w_r^* w_\theta + w_\theta^* w_r) \\ &= B_{11} |w_r|^2 + \frac{B_{22}}{r^2} |w_\theta|^2 + \frac{2B_{12}}{r} \Re\{ w_r^* w_\theta \}. \end{aligned} \tag{4.27}$$

Denote $A = t^{3/2}$, so $w = A e^{\mathrm{i}k\sigma_1 T}$ and $A = |w|$. Then, we find readily that

$$\begin{aligned} w_r &= (A_r + \mathrm{i}k\sigma_1 T_r A) e^{\mathrm{i}k\sigma_1 T} = \left(\frac{A_r}{A} + \mathrm{i}k\sigma_1 T_r \right) w, \\ w_\theta &= \left(\frac{A_\theta}{A} + \mathrm{i}k\sigma_1 T_\theta \right) w, \end{aligned} \tag{4.28}$$

so we have

$$
\begin{aligned}
&|w_r|^2 = \Big|\frac{A_r}{A} + \mathrm{i}k\sigma_1 T_r\Big|^2 |w|^2 = A_r^2 + k^2\sigma_1^2 T_r^2 A^2,\\
&|w_\theta|^2 = A_\theta^2 + k^2\sigma_1^2 T_\theta^2 A^2,\\
&\Re\{w_r^* w_\theta\} = A_r A_\theta + k^2\sigma_1^2 T_r T_\theta A^2,\\
&w_r^* w = AA_r - \mathrm{i}k\sigma_1 T_r A^2,\\
&w_\theta^* w = AA_\theta - \mathrm{i}k\sigma_1 T_\theta A^2.
\end{aligned}
\tag{4.29}
$$

Recall from (4.6) that

$$
B_{11} = \frac{S}{rS_r}\Big(1 + \frac{S_\theta^2}{S^2}\Big), \quad B_{12} = -\frac{S_\theta}{S}, \quad B_{22} = \frac{rS_r}{S}, \quad n = \frac{SS_r}{r}. \tag{4.30}
$$

Then inserting (4.29)–(4.30) into (4.27), we derive

$$
\begin{aligned}
(\breve{\nabla} w^*)^t \boldsymbol{B}\, \breve{\nabla} w &= \big(A_r^2 + k^2\sigma_1^2 T_r^2 A^2\big)\left(\frac{S}{rS_r} + \frac{S_\theta^2}{rSS_r}\right) + \frac{S_r}{rS}\big(AA_\theta + \mathrm{i}k\sigma_1 T_\theta A^2\big)\\
&\quad - \frac{2S_\theta}{rS}\big(A_r A_\theta + k^2\sigma_1^2 T_r T_\theta A^2\big)\\
&= \frac{S}{rS_r}\big(A_r^2 + k^2\sigma_1^2 T_r^2 A^2\big) + \frac{1}{rSS_r}\big(A_r^2 S_\theta^2 + A_\theta^2 S_r^2 - 2S_r S_\theta A_r A_\theta\big)\\
&\quad + \frac{k^2\sigma_1^2 A^2}{rSS_r}\big(T_r^2 S_\theta^2 + T_\theta^2 S_r^2 - 2S_r S_\theta T_r T_\theta\big)\\
&= \frac{S}{rS_r}\big(A_r^2 + k^2\sigma_1^2 T_r^2 A^2\big) + \frac{1}{rSS_r}\big(A_r S_\theta - A_\theta S_r\big)^2\\
&\quad + \frac{k^2\sigma_1^2 A^2}{rSS_r}\big(T_r S_\theta - T_\theta S_r\big)^2.
\end{aligned}
$$

By (4.14) and (4.30) and the above equation,

$$
\begin{aligned}
\breve{n} = (\breve{\nabla} w^*)^t \boldsymbol{B}\, \breve{\nabla} w - k^2\,|w|^2\, n &= A_r^2\frac{S}{rS_r} + k^2 A^2\left(\sigma_1^2 T_r^2\frac{S}{rS_r} - \frac{SS_r}{r}\right)\\
&\quad + \frac{1}{rSS_r}\big(A_r S_\theta - A_\theta S_r\big)^2 + k^2\sigma_1^2\frac{A^2}{rSS_r}\big(T_r S_\theta - T_\theta S_r\big)^2.
\end{aligned}
\tag{4.31}
$$

We have from (4.1)–(4.2) that in $\Omega_\varrho^{\mathrm{PAL}}$, $S = R_1 + \alpha T$, $R_2 = \varrho R_1$, and

$$
T = \frac{(R_2 - R_1)(r - R_1)}{R_2 - r}, \quad S_r = \alpha T_r, \quad S_\theta = R_1' + \alpha T_\theta. \tag{4.32}
$$

Moreover, from the expression of t in (4.19), we find immediately that

$$
A_r = \frac{3}{2}t^{\frac{1}{2}}t_r = -\frac{3\sigma_1}{2R_1}t^{\frac{5}{2}}T_r, \quad A_\theta = \frac{3}{2}t^{\frac{1}{2}}t_\theta = \frac{3\sigma_1 t^{\frac{5}{2}}}{2R_1}\left(\frac{R_1'}{R_1}T - T_\theta\right). \tag{4.33}
$$

Then by (4.32)–(4.33),

$$
\begin{aligned}
A_r S_\theta - A_\theta S_r &= -\frac{3\sigma_1}{2R_1}t^{\frac{5}{2}}T_r(R_1' + \alpha T_\theta) - \frac{3\sigma_1 t^{\frac{5}{2}}}{2R_1}\left(\frac{R_1'}{R_1}T - T_\theta\right)\alpha T_r\\
&= -\frac{3R_1'\sigma_1}{2R_1}t^{\frac{5}{2}}T_r\left(1 + \frac{\alpha T}{R_1}\right),
\end{aligned}
\tag{4.34}
$$

and

$$T_rS_\theta - T_\theta S_r = T_r(R_1' + \alpha T_\theta) - T_\theta(\alpha T_r) = R_1' T_r. \tag{4.35}$$

We now express $\breve{n}$ in terms of the regular functions $t, \beta, \tau, \gamma_1, \gamma_2$ in (4.19)–(4.20) as follows:

(4.36)
$$\begin{aligned}\breve{n} &= A_r^2 \frac{S}{rS_r} + k^2A^2\left(\sigma_1^2T_r^2\frac{S}{rS_r} - \frac{SS_r}{r}\right)\\ &\quad + \frac{1}{rSS_r}\frac{9R_1'^2\sigma_1^2}{4R_1^2}t^5T_r^2\left(1+\alpha\frac{T}{R_1}\right)^2 + k^2\sigma_1^2\frac{A^2}{rSS_r}R_1'^2T_r^2\\ &= \frac{9\gamma_1\sigma_1^2t^2}{4rR_1^2}\frac{\beta}{\alpha} + \frac{k^2\gamma_1}{r}\left(\sigma_1^2\frac{\beta}{\alpha} - \alpha\beta\right) + \frac{9\gamma_1\sigma_1^2R_1'^2t^2}{4rR_1^2\alpha\beta}\left(t+\frac{\alpha\tau}{R_1}\right)^2 + k^2\sigma_1^2\frac{R_1'^2\gamma_1t^2}{r\alpha\beta}.\end{aligned}$$

We obtain the identity (4.23) immediately by regrouping the terms.

(ii) Now, we calculate the elements of the vectors $\boldsymbol{p}$ and $\boldsymbol{q}$ in (4.13), that is,

$$\begin{aligned}\boldsymbol{p} = (p_1,p_2)^t &:= w\boldsymbol{B}\breve{\nabla}w^* = \boldsymbol{B}(\breve{\nabla}w^*w)\\ &= \left(B_{11}w_r^*w + B_{12}w_\theta^*w/r, B_{12}w_r^*w + B_{22}w_\theta^*w/r\right)^t.\end{aligned} \tag{4.37}$$

Then by (4.19)–(4.20), (4.29)–(4.30), and (4.34)–(4.35),

(4.38)
$$\begin{aligned}p_1 &= B_{11}w_r^*w + \frac{B_{12}}{r}w_\theta^*w\\ &= \frac{S}{rS_r}\left(1+\frac{S_\theta^2}{S^2}\right)\left(AA_r - \mathrm{i}k\sigma_1T_rA^2\right) - \frac{S_\theta}{rS}\left(AA_\theta - \mathrm{i}k\sigma_1T_\theta A^2\right)\\ &= \frac{S}{rS_r}\left(AA_r - \mathrm{i}k\sigma_1T_rA^2\right) + \frac{S_\theta A}{rSS_r}\left(A_rS_\theta - A_\theta S_r\right)\\ &\quad - \mathrm{i}k\sigma_1\frac{S_\theta A^2}{rSS_r}(T_rS_\theta - T_\theta S_r)\\ &= -\frac{\beta}{\alpha r}\left(\frac{3\sigma_1t}{2R_1} + \mathrm{i}k\sigma_1\right)t^2 - \frac{3R_1'\sigma_1}{2rR_1\alpha\beta}\left(t+\frac{\alpha\tau}{R_1}\right)(R_1't^2+\alpha\gamma_2)\,t^2\\ &\quad - \frac{\mathrm{i}k\sigma_1R_1'}{r\alpha\beta}(R_1't^2+\alpha\gamma_2)t^2\\ &= -\frac{\beta}{\alpha r}\left(\frac{3\sigma_1t}{2R_1} + \mathrm{i}k\sigma_1\right)t^2 - \left(\frac{3R_1'\sigma_1}{2rR_1\alpha\beta}\left(t+\frac{\alpha\tau}{R_1}\right) + \frac{\mathrm{i}k\sigma_1R_1'}{r\alpha\beta}\right)(R_1't^2+\alpha\gamma_2)t^2,\end{aligned}$$

and

$$\begin{aligned}p_2 &= B_{12}w_rw^* + \frac{B_{22}}{r}w_\theta w^*\\ &= -\frac{S_\theta}{S}\left(AA_r - \mathrm{i}k\sigma_1T_rA^2\right) + \frac{S_r}{S}\left(AA_\theta - \mathrm{i}k\sigma_1T_\theta A^2\right)\\ &= \frac{A}{S}\left(A_\theta S_r - A_rS_\theta\right) + \mathrm{i}k\sigma_1\frac{A^2}{S}(T_rS_\theta - T_\theta S_r)\\ &= \frac{3R_1'\gamma_1\sigma_1}{2R_1\beta}\left(t+\frac{\alpha\tau}{R_1}\right)t^2 + \mathrm{i}k\sigma_1\frac{R_1'\gamma_1}{\beta}t^2.\end{aligned} \tag{4.39}$$

Thus, we obtain (4.25).

We now turn to the elements of the vector $\boldsymbol{q}$. Note that

$$\begin{aligned}\boldsymbol{q} = (q_1, q_2)^t &:= w^* \boldsymbol{B} \breve{\nabla} w \\ &= \big(B_{11} w_r w^* + B_{12} w_\theta w^*/r, B_{12} w_r w^* + B_{22} w_\theta w^*/r\big)^t.\end{aligned} \tag{4.40}$$

Following the same lines as in (4.38)–(4.39), we find that q_1, q_2 are identical to p_1, p_2 with a change of $\mathrm{i}k$ therein to $-\mathrm{i}k$.

(iii) Finally, we deal with the matrix $\breve{\boldsymbol{B}}$, that is,

$$\breve{\boldsymbol{B}} = |w|^2 \boldsymbol{B} = \begin{pmatrix} \dfrac{t^3 S}{r S_r}\left(1 + \dfrac{S_\theta^2}{S^2}\right) & -\dfrac{t^3 S_\theta}{S} \\ -\dfrac{t^3 S_\theta}{S} & \dfrac{r t^3 S_r}{S} \end{pmatrix} := \begin{pmatrix} \breve{B}_{11} & \breve{B}_{12} \\ \breve{B}_{12} & \breve{B}_{22} \end{pmatrix}. \tag{4.41}$$

Using the notation in (4.20) and the properties in (4.32), we can derive the entries of $\breve{\boldsymbol{B}}$ in (4.24) straightforwardly. ∎

Remark 4.6. In the circular case, the artificial layer is an annulus, i.e.,

$$\Omega_\varrho^{\mathrm{PAL}} = \{R_1 < r < R_2 = \varrho R_1,\ 0 \le \theta < 2\pi\}, \tag{4.42}$$

where R_1 is independent of θ. Thus, R_1' and γ_2 in (4.20) reduce to 0. Consequently, several terms in (4.23)–(4.25) vanish and the variables involved in the sesquilinear form $\breve{\mathscr{B}}(v, \phi)$ in (4.22) are reduced to

$$\begin{aligned} &\breve{B}_{11} = \frac{\beta}{\alpha\gamma_1 r} t^4, \quad \breve{B}_{12} = 0, \quad \breve{B}_{22} = \frac{\alpha\gamma_1 r}{\beta} t^2, \\ &\breve{n} = k^2 \left(\frac{\beta\sigma_1^2}{\alpha} - \alpha\beta\right) \frac{\gamma_1}{r} + \frac{9\beta}{4\alpha} \frac{\gamma_1 \sigma_1^2}{r R_1^2} t^2, \\ &p_1 = -\frac{\beta\sigma_1}{\alpha r}\left(\frac{3t}{2R_1} + \mathrm{i}k\right) t^2, \quad p_2 = 0, \quad q_1 = -\frac{\beta\sigma_1}{\alpha r}\left(\frac{3t}{2R_1} - \mathrm{i}k\right) t^2, \quad q_2 = 0. \end{aligned} \tag{4.43}$$

Remark 4.7. For the circular PAL technique, it was shown in [53, Theorem 3] that for the transformed problem in (4.12) and (4.22) in the artificial annular layer, we have the Gårding-type inequality:

$$\begin{aligned}\Re\{\mathscr{B}_{\Omega_\varrho^{\mathrm{PAL}}}(u, u)\} = \Re\{\breve{\mathscr{B}}_{\Omega_\varrho^{\mathrm{PAL}}}(v, v)\} \ge ck^2 \int_0^{2\pi}\int_{R_1}^{R_2} \Theta(r)|v|^2 r dr d\theta \\ + \text{some weighted norms of } \partial_r v \text{ and } \partial_\theta v.\end{aligned}$$

Here, $\Theta(r) \ge 0$ for $R_1 < R_1^* \le r < R_2$, where R_1^* is some constant depending on the parameters and can approach to R_1 in the limiting case. Indeed, the PAL problem in the layers turns the indefinite problem in $(\tilde{r}, \tilde{\theta})$ into a nearly definite problem in (r, θ). However, the analysis for the general star-shaped truncation is much more involved, which we shall report in a separate work.

5. Numerical results and comparisons. In this section, we provide ample numerical results to illustrate the performance of the proposed PAL method, and also compare it with the PML_n and PML_∞ techniques using the ABFs in (3.22)–(3.23).

Consider the exterior scattering problem (3.1) with the domain truncated by a general star-shaped PAL layer. In all the following numerical tests, we choose

a plane wave $e^{\mathrm{i}kr\cos(\theta-\theta_0)}$ incident onto the scatterer D with an incident angle θ_0. Correspondingly, the boundary data g in (3.1) takes the form

$$g = -\exp\big(\mathrm{i}kR_0(\theta)\cos(\theta-\theta_0)\big), \tag{5.1}$$

given the parametric form of $\partial D : r = R_0(\theta), \theta = [0, 2\pi)$.

5.1. Circular PAL layer. We start with solving (3.1) with a circular scatterer D, so the exact solution is available as a series expansion

$$U(\boldsymbol{x}) = -\sum_{|m|=0}^{\infty} \frac{\mathrm{i}^m J_m(kR_0)}{H_m^{(1)}(kR_0)} H_m^{(1)}(kr) e^{\mathrm{i}m(\theta-\theta_0)}, \quad r > R_0. \tag{5.2}$$

The unbounded domain is truncated via an annular PAL layer. The numerical discretization is based on Theorem 4.5 with the coefficients give by (4.43). In light of the special geometry, we use the Fourier spectral approximation in the θ direction and the spectral-element method in the radial direction [47]. In the test, we fix $(R_0, R_1, R_2) = (1, 2, 2.2)$ and the incident angle $\theta_0 = 0$. Let M be the cut-off number of the Fourier modes, and let $\boldsymbol{N} = (N_1, N)$ be the highest polynomial degrees in the r-direction of two layers, respectively. The parameters in the mapping (3.11)–(3.12) are taken to be $\sigma_0 = \sigma_1 = 1$. We measure the maximum errors in Ω. We fix $N_1 = 300$ and $M = kR_1$ but vary N so that the waves in the interior layer can be well-resolved, and the error is dominated by the approximation in the outer annular layer.

In Figure 5, we compare the accuracy of the solvers with three techniques: PAL, PML_n (with $n = 1$, $\sigma_0 = (5.16, 2.78, 1.89, 1.43, 1.15, 1.01)$ for the wavenumber chosen as $k = (50, 100, 150, 200, 250, 300)$, respectively, which are optimal values as suggested in [10]), and PML_∞ ($\sigma_0 = 1/k$ as suggested in [8]) for various k. It can be seen from Figure 5(a) that when the wavenumber k is relatively small, the error curves (with $N < 20$) of these three methods intertwine with each other, and the error obtained by PML_∞ is slightly smaller than that of the other two methods. However, as N increases, the error for PML_∞ becomes much larger than that of the PAL and PML_n due to the large roundoff errors induced by the Gauss quadrature of singular functions. When k increases, the PAL method obviously outperforms its rivals, as depicted in Figures 5(b)–(f). For instance, the error of the PAL with $k = 150$ and $N = 20$ is around 10^{-8}, while those for the PML_n and PML_∞ are around $10^{-3} \sim 10^{-4}$. The comparison shows that the PAL method is apparently advantageous, especially when the wavenumber is large.

In practice, one would wish the artificial layer to be as thin as possible so that one can save computational cost for resolving the artificial unknowns in the layer. However, this might induce a boundary layer near the inner boundary, which brings about numerical difficulties in solving the resulting PAL- or PML-equations. As a result, a good balance of the layer thickness and the rate of decay is important, though it requires a delicate study of the dependence. Here, we provide some numerical evidence. We keep $R_1 = 2$ but let R_2 vary. In Table 1, we tabulate the numerical errors for fixed polynomial degrees $(N_1, N) = (300, 30)$ but for various $k = (10, 50, 100, 200, 300, 500)$. Observe that the thickness $d = R_2 - R_1$ indeed affects the accuracy. In Figure 6(a), we depict the errors against $k \times d$ for $k = 100, 200, 500$, which shows a good accuracy can be achieved when $kd \in [5, 25]$. The PAL works well when $\sigma_0 \approx 1$ and $\sigma_1 \leq 1$ as shown in Figures 6(b)–(c).

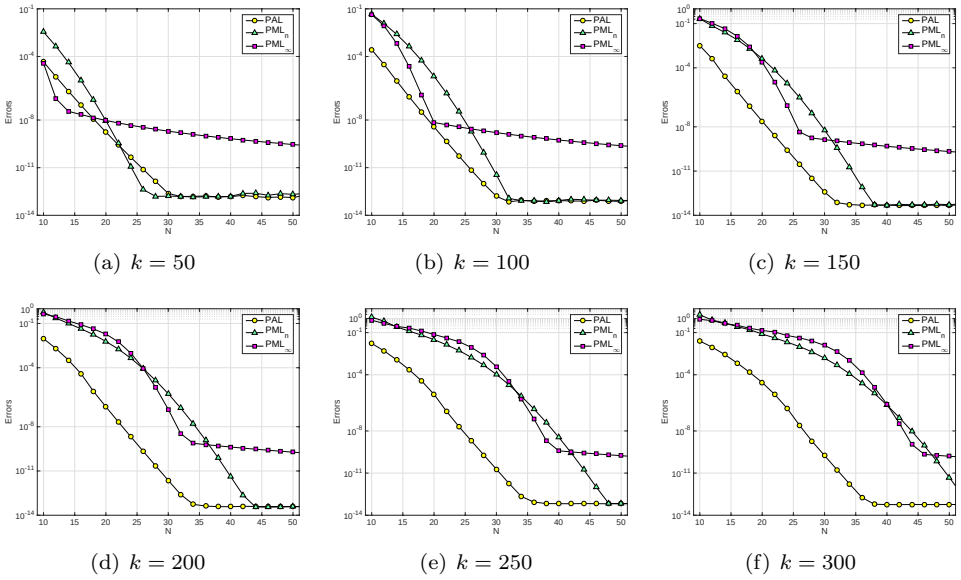

(a) $k = 50$ (b) $k = 100$ (c) $k = 150$

(d) $k = 200$ (e) $k = 250$ (f) $k = 300$

FIG. 5. *A comparison study: PAL versus PML_n versus PML_∞ for various $k = 50, 100, 150, 200, 250, 300$.*

TABLE 1
Errors versus thickness d for PAL with $(N_1, N) = (300, 30)$.

k	$d = 1$	$d = 0.5$	$d = 0.1$	$d = 0.01$	$d = 0.001$
10	1.11E-12	1.60E-12	1.26E-8	1.39E-4	1.69E-2
50	9.92E-11	4.67E-13	3.27E-12	2.82E-7	5.69E-4
100	2.65E-6	3.79E-11	2.08E-13	1.34E-8	8.65E-5
200	5.72E-4	1.91E-6	9.60E-14	3.12E-10	7.73E-6
300	3.60E-3	7.51E-5	2.65E-13	3.03E-11	1.30E-6
500	1.57E-2	1.40E-3	1.33E-11	1.90E-12	1.68E-7

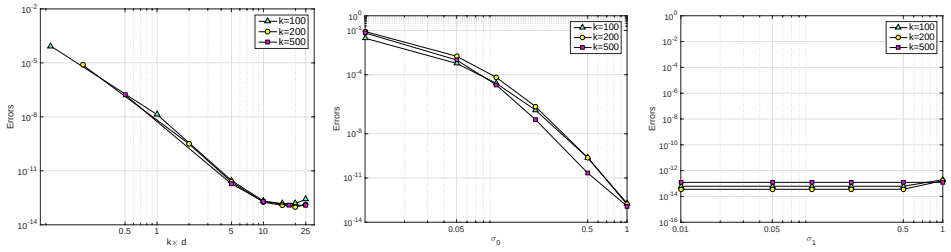

(a) errors against $k \times d$ (b) errors against σ_0 (c) errors against σ_1

FIG. 6. *Numerical errors against the thickness d and the parameters σ_0, σ_1 of the PAL layer obtained by a circular scatterer with a circular PAL layer.* (a) *Vary d with a fixed $\sigma_0 = \sigma_1 = 1$;* (b) *vary σ_0 with $d = 10/k$ and $\sigma_1 = 1$;* (c) *vary σ_1 with $d = 10/k$ and $\sigma_0 = 1$. The simulation results are obtained with $(R_0, R_1) = (1.0, 2.0)$, $(N_1, N) = (300, 30)$, $k = 100$, 200, 500, and $\theta_0 = 0$.*

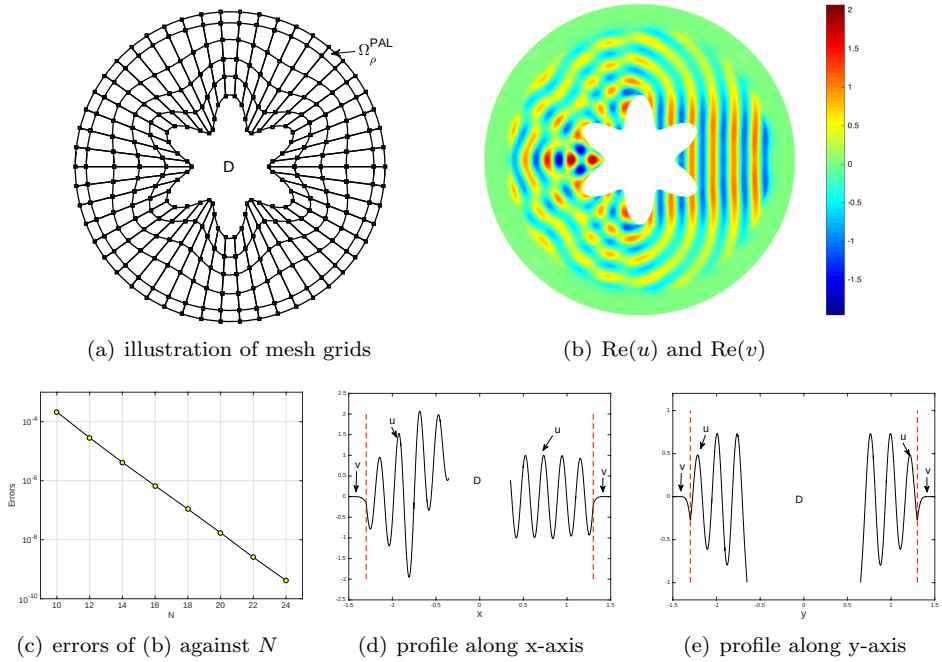

(a) illustration of mesh grids (b) Re(u) and Re(v)

(c) errors of (b) against N (d) profile along x-axis (e) profile along y-axis

FIG. 7. *Hexagonal star-shaped scatterer with an circular PAL layer. The simulation results are obtained with* $k = 30$, $\theta_0 = 0$, $\sigma_0 = \sigma_1 = 1$, $(R_1, R_2) = (1.3, 1.55)$, $N_1 = 35$ *and various* N.

Next, we consider a hexagonal star-shaped scatterer D whose boundary has the parametric form

$$R_0(\theta) = 0.5 + 0.15\sin(6(\theta + \pi/4)), \quad \theta = [0, 2\pi). \tag{5.3}$$

It is surrounded with an annular PAL layer with $(R_1, R_2) = (1.3, 1.55)$ (see Figure 7(a)). To numerically solve this problem, we discretize the computational domain with 250 nonoverlapping quadrilateral elements $\Omega = \{\Omega^{(i)}\}_{i=1}^{200}$ and $\Omega_\varrho^{\mathrm{PAL}} = \{\Omega_\varrho^{(i)}\}_{i=1}^{50}$, as shown in Figure 7(a). We adopt the spectral-element approximation based on the variational formulation in Theorem 4.5. Using the Gordon–Hall elemental transformation (cf. [56]) $\{T^i, T_\varrho^i\} : [-1, 1]^2 \mapsto \{\Omega^{(i)}, \Omega_\varrho^{(i)}\}$, we define the approximation space

$$\begin{aligned} u_{\boldsymbol{N}} \in V_{\boldsymbol{N}} = \big\{ & u \in H^1(\Omega) : u|_{\Omega^{(i)}} \circ T^i \in \mathbb{P}_{N_1} \times \mathbb{P}_{N_1}, \\ & u|_{\Omega_\varrho^{(i)}} = v_{\boldsymbol{N}} w,\ v_{\boldsymbol{N}}|_{\Omega_\varrho^{(i)}} \circ T_\varrho^i \in \mathbb{P}_{N_1} \times \mathbb{P}_N \big\}. \end{aligned} \tag{5.4}$$

We set $\theta_0 = 0$, $k = 30, \sigma_0 = \sigma_1 = 1$, and $N_1 = 35$ (which is sufficient to guarantee the numerical errors are mainly induced by the approximation in the PAL layer). Since the exact solution with an irregular scatterer is not available, we adopt the numerical solution obtained by $(N_1, N) = (35, 35)$ as a reference solution to obtain the numerical errors. In Figure 7(b), we plot $\Re\{u_{\boldsymbol{N}}\}|_\Omega$ and $\Re\{v_{\boldsymbol{N}}\}|_{\Omega_\varrho^{\mathrm{PAL}}}$ with $(N_1, N) = (35, 15)$. We plot the maximum errors in Ω against N in Figure 7(c). Observe that the errors decay exponentially as N increases, and the approximation in the layer has no oscillation and is well-behaved, as shown by the profiles along the x-axis and the y-axis of the numerical solution in Figures 7(d)–(e).

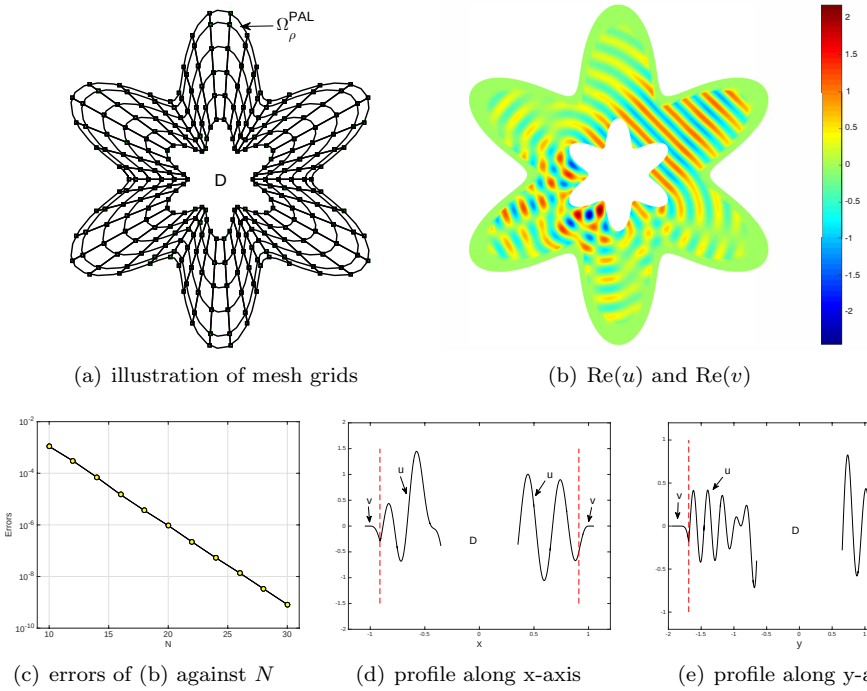

(a) illustration of mesh grids (b) Re(u) and Re(v)

(c) errors of (b) against N (d) profile along x-axis (e) profile along y-axis

FIG. 8. *Hexagonal star-shaped scatterer and PAL layer. The simulation results are obtained with* $k = 30$, $\theta_0 = \pi/4$, $\sigma_0 = \sigma_1 = 1$, $R_1(\theta) = 2.6R_0(\theta)$, *and* $R_2(\theta) = 3R_0(\theta)$ *with* $R_0(\theta)$ *defined in* (5.3), $N_1 = 35$, *and various* N.

5.2. Hexagonal star-shaped layer. Next, we surround the same scatterer as in Figure 7(a) with a hexagonal star-shaped layer, and the parametric forms of the inner and outer boundaries of the layer are $R_1(\theta) = 2.6R_0(\theta)$ and $R_2(\theta) = 3R_0(\theta)$, respectively, with $R_0(\theta)$ given by (5.3) (see Figure 8(a)). We take $k = 30$ and the incident angle $\theta_0 = \pi/4$. The computational domain is decomposed into 250 nonoverlapping quadrilateral curvilinear elements as illustrated in Figure 8(a). We depict $\Re\{u_{\boldsymbol{N}}\}|_\Omega$ and $\Re\{v_{\boldsymbol{N}}\}|_{\Omega_\varrho^{\mathrm{PAL}}}$ with $(N_1, N) = (35, 15)$ in Figure 8(b). The maximum errors in Ω against N are shown in Figure 8(c). It is evident that the errors decrease exponentially as N increases. Figures 8(d)–(e) show the profiles of the numerical solution in Figure 8(b) along the x-axis and the y-axis, from which we observe the solution profiles in the PAL layer decrease exponentially without any oscillation.

5.3. Elliptical layer. As a third example, we truncate the exterior problem (3.1) with a circular scatterer of radius $R_0 = 1/2$ by an elliptical artificial layer. Its inner boundary Γ_{R_1} is an ellipse of the form

$$\frac{x^2}{a^2} + \frac{y^2}{b^2} = 1 \quad \text{with} \quad a = 1.5\cosh(0.7),\ b = 1.5\sinh(0.7),$$

so its parametric form $R_1(\theta)$ can be obtained by (3.9), and that of the outer ellipse is $R_2(\theta) = \varrho R_1(\theta)$. We take $k = 30, \theta_0 = \pi/3$, $\sigma_0 = \sigma_1 = 1$, and $\varrho = 17/15$. The computational domain is divided into 200 nonoverlapping spectral elements shown in Figure 9(a). The numerical solution $\Re\{u_{\boldsymbol{N}}\}|_\Omega$ and $\Re\{v_{\boldsymbol{N}}\}|_{\Omega_\varrho^{\mathrm{PAL}}}$ obtained with

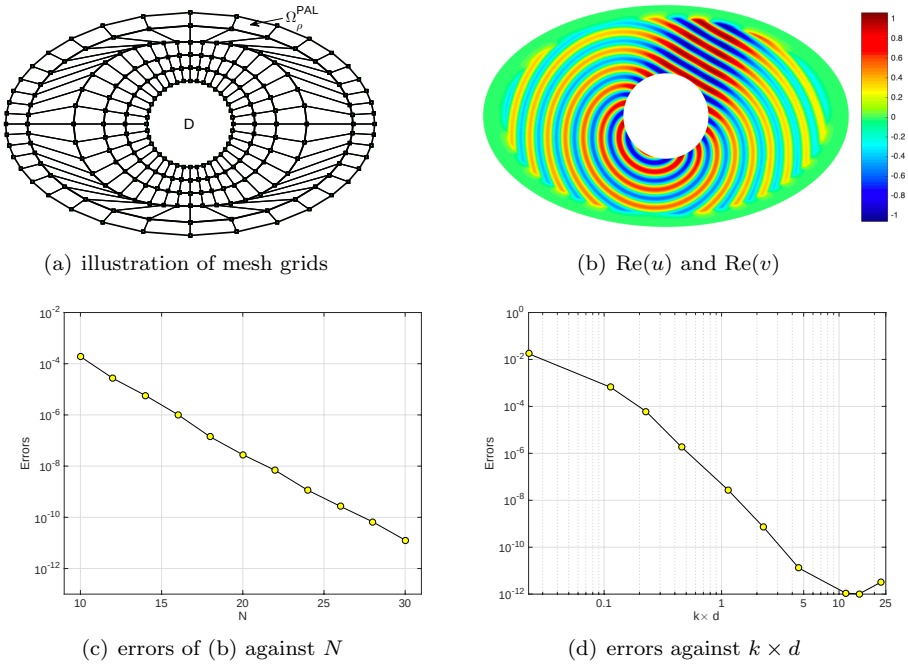

(a) illustration of mesh grids

(b) Re(u) and Re(v)

(c) errors of (b) against N

(d) errors against $k \times d$

FIG. 9. *A circular scatterer with elliptical PAL layer. The simulation results are obtained with* $k = 30$, $\theta_0 = \pi/3$, $N_1 = 35$, $\sigma_0 = \sigma_1 = 1$, $R_0 = 0.5$, $R_1(\theta)$ *is computed based on* (3.9). *The errors are plotted against* (i) *various* N *from* 10 *to* 30 *and a fixed* $R_2(\theta) = \frac{17}{15}R_1(\theta)$, *and* (ii) *various thickness* d *of the PAL layer and fixed* $N = 30$.

$(N_1, N) = (35, 15)$ is depicted in Figure 9(b). The maximum errors (compared with the exact solution (5.2)) against N are plotted in Figure 9(c). In Figure 9(d), we fix $N = 30$ and vary the thickness d of the elliptical PAL layer and plot the maximum errors against $k \times d$, similar to the test conducted for the circular PAL in Figure 7. Here, since the thickness of the elliptical layer depends on θ, we take $d := R_2(\frac{\pi}{2}) - R_1(\frac{\pi}{2})$. It is seen that the PAL with elliptical artificial layer works well in the range of $kd \in [5, 25]$, which turns out to be in accordance with the observation in the circular PAL case.

5.4. Rectangular layer. Consider a peanut-shaped scatterer D with the parametric form of the boundary:

$$R_0(\theta) = 0.5 + 0.25\sin(2(\theta + \pi/4)), \quad \theta = [0, 2\pi). \tag{5.5}$$

It is more practical to surround D by a rectangular layer where the boundary Γ_{R_1} is a rectangle with four vertices: $(a, b), (-a, b), (-a, -b), (a, -b)$ with $a = 1.5$ and $b = 0.75$. Thus, $R_1(\theta)$ can be obtained by (3.8) and we let $R_2(\theta) = \frac{17}{15}R_1(\theta)$. In this simulation, the wavenumber and incident angle are set to be $k = 30$ and $\theta_0 = \pi/3$. The domain of interest is discretized into 200 spectral elements, as depicted in Figure 10(a). We plot $\Re\{u_{\boldsymbol{N}}\}|_\Omega$ and $\Re\{v_{\boldsymbol{N}}\}|_{\Omega_\varrho^{\text{PAL}}}$ computed with $(N_1, N) = (35, 15)$, the maximum error compared with the reference solution obtained with $N_1 = N = 35$, and the profiles of the numerical solution along the x-axis and the y-axis in Figures 10(b)–(f), respectively. Observe that the error decreases exponentially as N increases, and the field in the rectangular PAL layer is well-behaved and decreases smoothly to zero without any oscillation.

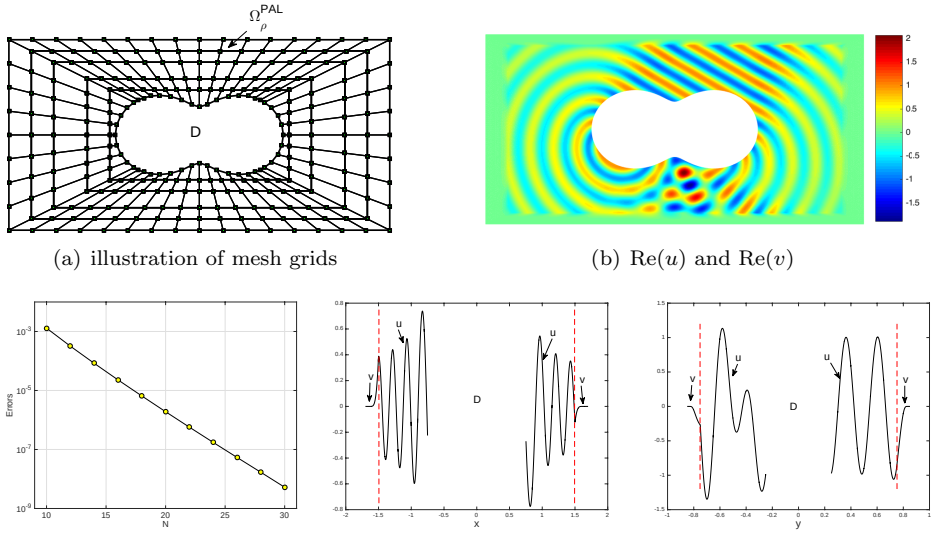

(a) illustration of mesh grids (b) Re(u) and Re(v)

(c) errors of (b) against N (d) profile along x-axis (e) profile along y-axis

FIG. 10. *Peanut-shaped scatterer with a rectangluar PAL layer. The simulation results are obtained with* $k = 30$, $\theta_0 = \pi/3$, $\sigma_0 = \sigma_1 = 1$, $R_0(\theta)$ *and* $R_1(\theta)$ *are computed based on* (5.5) *and* (3.8), *and* $R_2(\theta) = \frac{17}{15}R_1(\theta)$. *Here,* $N_1 = 35$.

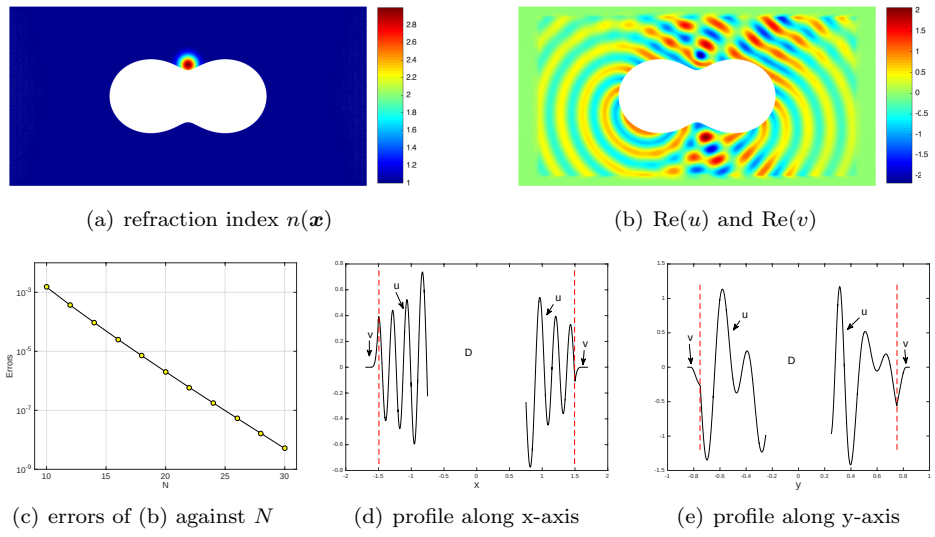

(a) refraction index $n(\boldsymbol{x})$ (b) Re(u) and Re(v)

(c) errors of (b) against N (d) profile along x-axis (e) profile along y-axis

FIG. 11. *Scattering problem with a locally inhomogeneous medium with a rectangular PAL. The simulation results are obtained with* $k = 30$, $\theta_0 = \pi/3$, $\sigma_0 = \sigma_1 = 1$, $R_0(\theta)$ *and* $R_1(\theta)$ *are computed based on* (5.5) *and* (3.8), *and* $R_2(\theta) = \frac{17}{15}R_1(\theta)$, $N_1 = 35$, *and various* N.

It is also of interest to simulate the exterior scattering problem with a locally inhomogeneous medium. All the numerical settings are the same except that the refraction index $n(\boldsymbol{x})$ in Theorems 4.3 and 4.5 in Ω is replaced by a shifted Gaussian function

$$n(\boldsymbol{x}) = 1 + c_0 \exp\left(-\frac{(x-x_0)^2 + (y-y_0)^2}{2c_1^2}\right) \tag{5.6}$$

with $x_0 = 0, y_0 = 0.3, c_0 = 2$, and $c_1 = 0.06$ (see Figure 11(a)). We depict in Figure 11(b) the real part of the numerical solution. Compared with the result with a homogeneous medium in Figure 10(b), the oscillation of the waves above the upper-middle region of the peanut scatterer increases, due to the influence of the inhomogeneity around this region. The maximum error and the profiles of the numerical solution along the x-axis and the y-axis are depicted in Figures 11(c)–(f), respectively, which demonstrate that the proposed PAL technique is accurate and robust for various scatterers with locally inhomogeneous media.

Appendix A. Proof of Theorem 2.1. For clarity, we first consider (2.1) with $g(y) = \hat{g}_l \sin(ly)$, and then apply the principle of superposition to obtain (2.10). Note that by (2.3), the exact solution of (2.1) is

$$U_l(x,y) = \hat{g}_l\, e^{\mathrm{i}\hat{k}_l x} \sin(ly), \tag{A.1}$$

and the PML-solution of (2.7)–(2.8) is

$$U_{\mathrm{p},l}(x,y) = \frac{e^{\mathrm{i}\hat{k}_l(S_d - S)} - e^{-\mathrm{i}\hat{k}_l(S_d - S)}}{e^{\mathrm{i}\hat{k}_l S_d} - e^{-\mathrm{i}\hat{k}_l S_d}}\, \hat{g}_l \sin(ly). \tag{A.2}$$

In fact, one verifies directly that (A.2) satisfies the PML-equation (2.7) and all conditions in (2.8)–(2.9). Since $S(x) = x$ for $x \in (0, L)$, we find

$$U_{\mathrm{p},l}(x,y) = \frac{e^{\mathrm{i}\hat{k}_l(S_d - 2x)} - e^{-\mathrm{i}\hat{k}_l S_d}}{e^{\mathrm{i}\hat{k}_l S_d} - e^{-\mathrm{i}\hat{k}_l S_d}}\, U_l(x,y) = (1 - R_l(x))\, U_l(x,y) \quad \forall\, (x,y) \in \Omega, \tag{A.3}$$

where the representation of $R_l(x)$ in (2.10) can be obtained straightforwardly. Thanks to the identity (A.3), we derive from the principle of superposition, (2.3), and (A.1) that the PML-solution in Ω is given by

$$U_{\mathrm{p}}(x,y) = \sum_{l=1}^{\infty} U_{\mathrm{p},l}(x,y) = U(x,y) - \sum_{l=1}^{\infty} \hat{g}_l\, R_l(x)\, e^{\mathrm{i}\hat{k}_l x} \sin(ly), \tag{A.4}$$

which yields (2.10).

It remains to derive the bounds in (2.12). One verifies readily that for $z = \alpha + \beta\,\mathrm{i}$ with $\alpha, \beta \in \mathbb{R}$,

$$|1 - e^{\alpha}| \le |1 - e^{z}| \le 1 + e^{\alpha}, \quad |\sin z| = \left|\frac{e^{\mathrm{i}z} - e^{-\mathrm{i}z}}{2\mathrm{i}}\right| = \frac{e^{-\beta}}{2}|1 - e^{-2\mathrm{i}z}|. \tag{A.5}$$

Then we have

$$|1 - e^{2\mathrm{Im}\{\hat{k}_l S_d\}}| \le |1 - e^{-2\mathrm{i}\hat{k}_l S_d}| \le 1 + e^{2\mathrm{Im}\{\hat{k}_l S_d\}}. \tag{A.6}$$

Therefore, (i) for $k > l$ (note $\hat{k}_l = \sqrt{k^2 - l^2}$), we obtain (2.12) from (A.5)–(A.6) immediately.

On the other hand, (ii) for $k < l$ (note $\hat{k}_l = \mathrm{i}|\hat{k}_l|$), the lower and upper bounds in (2.13) are a direct consequence of (A.6).

If k is a positive integer, we find that for the mode $l = k$, (A.1) is still valid (i.e., $U_l = \hat{g}_l \sin(ly)$), while (A.2) becomes

$$U_{\mathrm{p},l}(x,y) = \left(1 - \frac{S(x)}{S_d}\right) \hat{g}_l \, \sin(ly). \tag{A.7}$$

Thus, for the mode $l = k$, $R_l(x)$ should be replaced by $R_l(x) = -S(x)/S_d$ in the identity (2.10).

Appendix B. Proof of Theorem 4.2.

Proof. Without loss of generality, we start with a general nonsingular Cartesian coordinate transformation $\tilde{x} = X(x,y)$, $\tilde{y} = Y(x,y)$ with the Jacobian and Jacobian matrix given by

$$\boldsymbol{J} = \frac{\partial(x,y)}{\partial(\tilde{x},\tilde{y})} = \det(\boldsymbol{J}) \begin{pmatrix} Y_y & -X_y \\ -Y_x & X_x \end{pmatrix}, \quad \det(\boldsymbol{J}) = 1/(X_x Y_y - X_y Y_x). \tag{B.1}$$

It is known from the standard textbook that (4.3) can be transformed into

$$\mathcal{H}[U] = \frac{1}{n}\big\{\nabla \cdot (\boldsymbol{C}\, \nabla U) + k^2 n\, U\big\}, \tag{B.2}$$

where $U(x,y) = \tilde{U}(\tilde{x},\tilde{y})$ and

$$\boldsymbol{C} = \begin{pmatrix} C_{11} & C_{12} \\ C_{12} & C_{22} \end{pmatrix} = \frac{\boldsymbol{J}\,\boldsymbol{J}^t}{\det(\boldsymbol{J})}, \quad n = \frac{1}{\det(\boldsymbol{J})}. \tag{B.3}$$

To represent $\boldsymbol{J}$ and its determinant in polar coordinates, we rewrite the above nonsingular transformation as $\tilde{r} = R(r,\theta)$, $\tilde{\theta} = \Theta(r,\theta)$. Then by the chain rule, we have

$$\frac{\partial(x,y)}{\partial(\tilde{x},\tilde{y})}\frac{\partial(\tilde{x},\tilde{y})}{\partial(x,y)} = \frac{\partial(\tilde{x},\tilde{y})}{\partial(\tilde{r},\tilde{\theta})}\frac{\partial(\tilde{r},\tilde{\theta})}{\partial(\tilde{x},\tilde{y})} = \frac{\partial(r,\theta)}{\partial(x,y)}\frac{\partial(x,y)}{\partial(r,\theta)} = \boldsymbol{I}_2.$$

As a result, the matrix $\boldsymbol{J}$ can be computed by

$$\begin{aligned} \boldsymbol{J} = \frac{\partial(x,y)}{\partial(\tilde{x},\tilde{y})} &= \left(\frac{\partial(\tilde{x},\tilde{y})}{\partial(x,y)}\right)^{-1} = \left(\frac{\partial(\tilde{x},\tilde{y})}{\partial(\tilde{r},\tilde{\theta})}\frac{\partial(\tilde{r},\tilde{\theta})}{\partial(r,\theta)}\frac{\partial(r,\theta)}{\partial(x,y)}\right)^{-1} \\ &= \frac{\partial(x,y)}{\partial(r,\theta)}\left(\frac{\partial(\tilde{r},\tilde{\theta})}{\partial(r,\theta)}\right)^{-1}\frac{\partial(\tilde{r},\tilde{\theta})}{\partial(\tilde{x},\tilde{y})}. \end{aligned} \tag{B.4}$$

Straightforward calculation leads to

$$\frac{\partial(x,y)}{\partial(r,\theta)} = \boldsymbol{T}(\theta)\begin{pmatrix} 1 & 0 \\ 0 & r \end{pmatrix}, \quad \frac{\partial(\tilde{r},\tilde{\theta})}{\partial(\tilde{x},\tilde{y})} = \begin{pmatrix} 1 & 0 \\ 0 & 1/\tilde{r} \end{pmatrix}\boldsymbol{T}^t(\tilde{\theta}) \tag{B.5}$$

and

$$\frac{\partial(\tilde{r},\tilde{\theta})}{\partial(r,\theta)} = \begin{pmatrix} R_r & R_\theta \\ \Theta_r & \Theta_\theta \end{pmatrix}, \quad \left(\frac{\partial(\tilde{r},\tilde{\theta})}{\partial(r,\theta)}\right)^{-1} = \frac{1}{R_r\Theta_\theta - R_\theta\Theta_r}\begin{pmatrix} \Theta_\theta & -R_\theta \\ -\Theta_r & R_r \end{pmatrix}. \tag{B.6}$$

Inserting (B.5)–(B.6) into (B.4), and using the property $\det(\boldsymbol{T}(\theta)) = \det(\boldsymbol{T}(\tilde{\theta})) = 1$, we find

$$\det(\boldsymbol{J}) = \frac{r}{R(R_r\Theta_\theta - R_\theta\Theta_r)}, \quad \boldsymbol{J} = \det(\boldsymbol{J})\,\boldsymbol{T}(\theta)\begin{pmatrix} R\Theta_\theta/r & -R_\theta/r \\ -R\Theta_r & R_r \end{pmatrix}\boldsymbol{T}^t(\Theta). \tag{B.7}$$

We now apply the above general formulas to (4.1), that is, $\tilde{r} = R = S(r,\theta)$, $\tilde{\theta} = \Theta = \theta$, so $R_r = S_r, R_\theta = S_\theta, \Theta_r = 0, \Theta_\theta = 1$. Then we obtain immediately from (B.7) that

$$\det(\boldsymbol{J}) = \frac{r}{SS_r}, \quad \boldsymbol{J} = \boldsymbol{T}(\theta) \begin{pmatrix} \frac{1}{S_r} & -\frac{S_\theta}{SS_r} \\ 0 & \frac{r}{S} \end{pmatrix} \boldsymbol{T}^t(\theta). \tag{B.8}$$

Then, $\boldsymbol{C}$ and n in (4.5) can be derived directly from (B.3) and (B.8). This ends the proof. ∎

REFERENCES

[1] M. Abramovitz and I. A. Stegun, *Handbook of Mathematical Functions*, Dover, New York, 1972.

[2] S. Amini and S. M. Kirkup, *Solution of Helmholtz equation in the exterior domain by elementary boundary integral methods*, J. Comput. Phys., 118 (1995), pp. 208–221.

[3] A. Bayliss and E. Turkel, *Radiation boundary conditions for wave-like equations*, Commun. Pure Appl. Math., 33 (1980), pp. 707–725.

[4] J. P. Bérenger, *A perfectly matched layer for the absorption of electromagnetic waves*, J. Comput. Phys., 114 (1994), pp. 185–200.

[5] J. P. Bérenger, *Perfectly matched layer for the FDTD solution of wave-structure interaction problems*, IEEE Trans. Antennas Propag., 44 (1996), pp. 110–117.

[6] J. P. Bérenger, *Three-dimensional perfectly matched layer for the absorption of electromagnetic waves*, J. Comput. Phys., 114 (1996), pp. 363–379.

[7] A. Bermúdez, L. Hervella-Nieto, A. Prieto, and R. Rodríguez, *An exact bounded perfectly matched layer for time-harmonic scattering problems*, SIAM J. Sci. Comput., 30 (2007), pp. 312–338.

[8] A. Bermúdez, L. Hervella-Nieto, A. Prieto, and R. Rodríguez, *An optimal perfectly matched layer with unbounded absorbing function for time-harmonic acoustic scattering problems*, J. Comput. Phys., 223 (2007), pp. 469–488.

[9] J. P. Boyd, *Chebyshev and Fourier Spectral Methods*, 2nd ed., Dover, New York, 2001.

[10] Z. M. Chen and X. Z. Liu, *An adaptive perfectly matched layer technique for time-harmonic scattering problems*, SIAM J. Numer. Anal., 43 (2005), pp. 645–671.

[11] Z. M. Chen and X. M. Wu, *An adaptive uniaxial perfectly matched layer method for time-harmonic scattering problems*, Numer. Math. Theory Methods Appl., 1 (2008), pp. 113–137.

[12] Z. M. Chen, T. Cui, and L. B. Zhang, *An adaptive anisotropic perfectly matched layer method for 3-D time harmonic electromagnetic scattering problems*, Numer. Math., 125 (2013), pp. 639–677.

[13] Z. M. Chen and W. Y. Zheng, *PML method for electromagnetic scattering problem in a two-layer medium*, SIAM J. Numer. Anal., 55 (2017), pp. 2050–2084.

[14] W. C. Chew and W. H. Weedon, *A 3D perfectly matched medium from modified Maxwell's equations with stretched coordinates*, Microw. Opt. Technol. Lett., 7 (1994), pp. 599–604.

[15] R. Cimpeanu, A. Martinsson, and M. Heil, *A parameter-free perfectly matched layer formulation for the finite-element-based solution of the Helmholtz equation*, J. Comput. Phys., 296 (2015), pp. 329-347.

[16] F. Collino and P. Monk, *The perfectly matched layer in curvilinear coordinates*, SIAM J. Sci. Comput., 19 (1998), pp. 2061–2090.

[17] D. Colton and R. Kress, *Integral Equation Methods in Scattering Theory*, Classics in Appl. Math. 72, SIAM, Philadelphia, 2013.

[18] A. Darvish, B. Zakeri, and N. Radkani, *An optimized hybrid convolutional perfectly matched layer for efficient absorption of electromagnetic waves*, J. Comput. Phys., 356 (2018), pp. 31–45.

[19] C. Deng, M. Luo, M. Yuan, B. Zhao, M. Zhuang, and Q. H. Liu, *The auxiliary differential equations perfectly matched layers based on the hybrid SETD and PSTD algorithms for acoustic waves*, J. Comput. Acoustics, 26 (2017), 1750031.

[20] M. O. Deville, P. F. Fischer, and E. H. Mund, *High-Order Methods for Incompressible Fluid Flow*, Cambridge Monogr. Appl. Comput. Math. 9, Cambridge University Press, Cambridge, UK, 2002.

[21] B. Engquist and A. Majda, *Absorbing boundary conditions for numerical simulation of waves*, Math. Comp., 31 (1977), pp. 629–651.
[22] K. Feng, *Finite element method and natural boundary reduction*, in Proceeding of ICM, Warsaw, 1983, pp. 1439–1453.
[23] N. Feng, Y. Yue, C. Zhu, L. Wan, and Q. H. Liu, *Second-order PML: Optimal choice of nth-order PML for truncating FDTD domains*, J. Comput. Phys., 285 (2015), pp. 71–83.
[24] A. Fournier, *Exact calculation of Fourier series in nonconforming spectral-element methods*, J. Comput. Phys., 215 (2006), pp. 1–5.
[25] D. Givoli, *Non-reflecting boundary conditions*, J. Comput. Phys., 94 (1991), pp. 1–29.
[26] D. Givoli, *High-order non-reflecting boundary scheme for time-dependent waves*, J. Comput. Phys., 186 (2003), pp. 24–46.
[27] C. I. Goldstein, *A finite element method for solving Helmholtz type equations in waveguides and other unbounded domains*, Math. Comp., 39 (1982), pp. 309–324.
[28] W. J. Gordon and C. A. Hall, *Transfinite element methods: Blending-function interpolation over arbitrary curved element domains*, Numer. Math., 21 (1973), pp. 109–129.
[29] B. Y. Guo, *Gegenbauer approximation and its applications to differential equations with rough asymptotic behaviors at infinity*, Appl. Numer. Math., 38 (2001), pp. 403–425.
[30] T. Hagstrom, *Radiation boundary conditions for the numerical simulation of waves*, Acta Numer., 8 (1999), pp. 47–106.
[31] T. Hagstrom, D. Givoli, D. Rabinovich and J. Bielak, *The double absorbing boundary method*, J. Comput. Phys., 259 (2014), pp. 220–241.
[32] T. Hagstrom and L. Stephen, *Radiation boundary conditions for Maxwell's equations: A review of accurate time-domain formulations*, J. Comput. Math., 25 (2007), pp. 305–336.
[33] S. Johnson, *Notes on Perfectly Matched Layers*, Technical report, Massachusetts Institute of Technology, Cambridge, MA, 2010.
[34] S. N. Karp, *A convergent 'farfield' expansion for two-dimensional radiation functions*, Commun. Pure Appl. Math., 14 (1961), pp. 427–434.
[35] M. Lassas and E. Somersalo, *On the existence and convergence of the solution of PML equations*, Computing, 60 (1998), pp. 229–241.
[36] Y. Li and H. Wu, *FEM and CIP-FEM for Helmholtz equation with high wave number and perfectly matched layer truncation*, SIAM J. Numer. Anal., 57 (2019), pp. 96–126.
[37] P. Loh, A. Oskooi, M. Ibanescu, M. Skorobogatiy, and S. Johnson, *Fundamental relation between phase and group velocity, and application to the failure of perfectly matched layers in backward-wave structures*, Phys. Rev. E, 79 (2009), 065601.
[38] D. Nicholls and F. Reitich, *Stability of high-order perturbative methods for the computation of Dirichlet-Neumann operators*, J. Comput. Phys., 170 (2001), pp. 276–298.
[39] D. Nicholls and N. Nigam, *Exact non-reflecting boundary conditions on general domains*, J. Comput. Phys., 194 (2004), pp. 278–303.
[40] D. Nicholls and J. Shen, *A stable high-order method for two-dimensional bounded-obstacle scattering*, SIAM J. Sci. Comput., 28 (2006), pp. 1398–1419.
[41] J. B. Pendry, D. Schurig, and D. R. Smith, *Controlling electromagnetic fields*, Science, 312 (2006), pp. 1780–1782.
[42] A. Modave, E. Delhez, and C. Geuzaine, *Optimizing perfectly matched layers in discrete contexts*, Internat. J. Numer. Methods Engrg., 99 (2014), pp. 410–437.
[43] J. C. Nédélec, *Acoustic and Electromagnetic Equations*, Springer-Verlag, New York, 2001.
[44] D. Rabinovich, D. Givoli, and E. Bécache, *Comparison of high-order absorbing boundary conditions and perfectly matched layers in the frequency domain*, Internat. J. Numer. Methods. Engrg., 26 (2010), pp. 1351–1369.
[45] D. Rabinovich, D. Givoli, J. Bielak, and T. Hagstrom, *The double absorbing boundary method for a class of anisotropic elastic media*, Comput. Methods Appl. Mech. Engrg., 315 (2017), pp. 190–221.
[46] C. Radu, M. Anton, and H. Matthias, *A parameter-free perfectly matched layer formulation for the finite-element-based solution of the Helmholtz equation*, J. Comput. Phys., 296 (2015), pp. 329–347.
[47] J. Shen, T. Tang, and L. L. Wang, *Spectral Methods: Algorithms, Analysis and Applications*, Springer Ser. Comput. Math. 41, Springer, Berlin, 2011.
[48] J. Shen and L. L. Wang, *Some recent advances on spectral methods for unbounded domains*, Commun. Comput. Phys., 5 (2009), pp. 195–241.
[49] I. Singer and E. Turkel, *A perfectly matched layer for the Helmholtz equation in a semi-infinite strip*, J. Comput. Phys., 201 (2004), pp. 439–465.
[50] Q. Sun, R. Zhang, Q. Zhan, and Q. H. Liu, *A novel coupling algorithm for perfectly matched layer with wave equation-based discontinuous Galerkin time-domain method*, IEEE Trans. Antennas Propag., 66 (2018), pp. 255–261.

[51] A. Taflove and S. Hagness, *Computational Electrodynamics: The Finite-Difference Time-Domain Method*, 3rd ed., Artech House, Boston, MA, 2005.
[52] B. Wang, L. L. Wang, and Z. Xie, *Accurate calculation of spherical and vector spherical harmonic expansions via spectral element grids*, Adv. Comput. Math., 44 (2018), 951–985.
[53] L. L. Wang and Z. G. Yang, *A perfect absorbing layer for high-order simulation of wave scattering problems*, in Spectral and High Order Methods for Partial Differential Equations, M. L. Bittencourt et al. eds., Springer, New York, 2017, pp. 81–101.
[54] W. Yang, J. Li, and Y. Huang, *Mathematical analysis and finite element time domain simulation of arbitrary star-shaped electromagnetic cloaks*, SIAM J. Numer. Anal., 56 (2018), pp. 136–159.
[55] Z. G. Yang and L. L. Wang, *Accurate simulation of circular and elliptic cylindrical invisibility cloaks*, Commun. Comput. Phys., 17 (2015), pp. 822–849.
[56] Z. G. Yang, L. L. Wang, Z. J. Rong, B. Wang, and B. L. Zhang, *Seamless integration of global Dirichlet-to-Neumann boundary condition and spectral elements for transformation electromagnetics*, Comput. Methods Appl. Mech. Engrg., 301 (2016), pp. 137–163.
[57] N. A. Zharova, L. V. Shadrivov, and Y. S. Kivshar, *Inside-out electromagnetic cloaking*, Opt. Express, 16 (2008), pp. 4615–4620.
[58] W. Zhou and H. Wu, *An adaptive finite element method for the diffraction grating problem with PML and few-mode DtN truncations*, J. Sci. Comput., 76 (2018), pp. 1813–1838.